*J. Fluid Mech.* (1987), *vol.* 175, *pp.* 1–41
*Printed in Great Britain*

# A study of hairpin vortices in a laminar boundary layer. Part 1. Hairpin vortices generated by a hemisphere protuberance

By M. S. ACARLAR
AT&T Bell Laboratories, Allentown, PA 18015, USA

AND C. R. SMITH
Dept. of Mechanical Engineering and Mechanics, Lehigh University,
Bethlehem, PA 18015, USA

(Received 7 October 1985 and in revised form 27 May 1986)

It has been suggested that hairpin vortices may play a key role in developing and sustaining the turbulence process in the near-wall region of turbulent boundary layers. To examine this suggestion, a study was done of the hairpin vortices generated by the interaction of a hemisphere protuberancee within a developing laminar boundary layer. Under the proper conditions, hairpin vortices are shed extremely periodically, which allows detailed examination of their behaviour. Shedding characteristics of the hemispheres were determined using hot-film-anemometry techniques. The flow patterns created by the presence of the hairpin vortices have been documented using flow visualization and hot-film-anemometry techniques, and cross-compared with the patterns observed in the near-wall of a fully turbulent boundary layer. In general, it has been observed that many of the visual patterns observed in the near-wall region of a turbulent boundary layer can also be observed in the wake of the hairpin-shedding hemisphere, which appears supportive of the importance of hairpin vortices in the near-wall turbulence production process. Furthermore, velocity measurements indicate the presence of strong inflexional profiles just downstream of the hairpin-vortex generation region which evolve into fuller profiles with downstream distance, eventually developing a remarkable similarity to a turbulent-boundary-layer velocity profile.

---

## 1. Introduction

To facilitate an examination of the potential of hairpin (or horseshoe) vortices as the possible source of many flow characteristics in the near-wall region of turbulent boundary layers, a study of discrete hairpin vortices and their induced flow patterns in an initially stable laminar boundary layer was undertaken. The initial approach to this study is based on some observations by Metzler (1980), who observed that under certain conditions symmetric, controlled horseshoe or hairpin vortices are generated in the separated laminar wake behind a hemisphere. Although it has long been known that spheres placed in either a uniform flow or a shear flow will shed hairpin-type vortices under certain flow conditions, there is limited information on the detailed behavioural characteristics of such vortices.

Numerous researchers have studied the vortex-shedding characteristics due to uniform flow past spheres. Möller (1938) employed stereoscopic cinematography to record the flow behaviour behind a sphere being steadily towed through water at

Reynolds numbers between 150 and 10000. He observed that vortex-ring formation and shedding began at $Re_d \approx 450$, with these vortices shed 180° apart, giving the impression of being linked together in a 'vortex chain'. At a Reynolds number of about 1000 discrete vortices appeared. These vortices were unstable and appeared to join together to form periodic 'balls of vorticity' or 'wirbelvolken'. The reader is referred to Taneda (1956), Torobin & Gauvin (1959), and Achenbach (1974) for reviews of experimental and theoretical work dealing with the wakes of spheres.

In addition to work on shedding behaviour in uniform flows, several studies have been done of transition due to protuberances placed beneath initially laminar boundary layers. Klebanoff (1955), Dryden (1953) and Tani (1961) established the conditions for which transition from laminar to turbulent flow occurred due to single two- and three-dimensional elements placed beneath an initially laminar boundary layer. Further hot-wire studies by Klebanoff, Tidstrom & Sargent (1962) illustrate that an isolated hemispherical roughness element will, under appropriate conditions, shed eddies that yield velocity profiles which are remarkably similar to those observed at wave breakdown during laminar transition. The effects of surface-mounted proturberances in promoting three-dimensional boundary-layer transition, and the subsequent observation of hairpin-loop formation during transition, have been discussed more recently by Tani (1981).

Mochizuki (1961*a*) studied the transition and resulting flow patterns induced by spheres attached to a flat plate beneath a developing laminar boundary layer. Using smoke visualization, it was observed that at low velocities streamwise vortex filaments formed in the sphere wake. With increasing velocity, these vortex filaments began to periodically deform such that a row of loop-shaped (hairpin) vortices was formed. As the velocity was further increased, a wedge-shaped turbulent region appeared downstream and gradually approached the sphere. However, Mochizuki did not examine the individual behaviour of the hairpin vortices, although a parallel study using hot-film-anemometry measurements (Mochizuki 1961*b*) demonstrates details of the mean-flow changes induced by the presence of these hairpin streets.

Hall (1967) examined the transition induced by small bluff bodies, including spheres, which were suspended at various heights above a flat surface within a developing boundary layer. He observed that laminar-to-turbulent transition of the boundary layer occurs above a certain 'critical' element Reynolds number which is based on the velocity at the tip of the element and the diameter of the element. Below this Reynolds number, vortices that were shed decayed as they propagated downstream. Comparing the wavelengths of the shed vortices with the minimum unstable wavelengths of two-dimensional disturbances for a similar undisturbed laminar boundary layer (from classical stability theory), Hall concluded that the mechanism by which laminar to turbulent transition occurred was dependent upon the stability characteristics of the element wake rather than the stability characteristics of the boundary layer.

In summary, the state of knowledge of the hairpin flow structures generated by flow over surface protuberances is limited, consisting primarily of qualitative observations and some limited velocity information. The details of the generation, evolution and interaction of hairpin vortices are still very much in question.

Thus, to develop a comprehensive understanding of the behaviour of hairpin-type vortices, the present study had the following objectives:

(i) to determine the shedding conditions and detailed characteristics of hairpin vortices generated in the wake of hemisphere protuberances placed on a flat plate beneath an initially laminar boundary layer;

(ii) to establish the behaviour of hairpin vortices throughout their formation and evolution;
(iii) to examine any secondary structures that these hairpin vortices generate;
(iv) to establish flow-visualization patterns that characterize the various portions of both the hairpin vortices and the secondary structures that they generate;
(v) to illustrate the similarities between the flow-visualization patterns created by the presence of hairpin vortices generated by a hemisphere protuberance and the patterns observed in the wall region of turbulent boundary layers.

## 2. Experimental equipment and techniques

The present experiments were all carried out in a recirculating, free-surface Plexiglas water channel. Hairpin vortices were generated by three-dimensional vortex shedding from hemispheres and half-teardrop protuberances placed beneath an initially laminar boundary layer. Dye and hydrogen-bubble-wire flow-visualization techniques were utilized extensively in combination with an INSTAR high-speed (120 frames/s) video system for visualization studies. A Digital Equipment Corporation PDP 11/23 data acquisition system was used for hot-film-data recording, storage and processing. See Acarlar & Smith (1984) for details of the systems.

The water-channel system has a working section 5 m long, 0.9 m wide, and 0.35 m deep. Utilizing a combination of honeycomb flow-straightener and 20-mesh stainless-steel screens, a maximum turbulence intensity of 0.2 % was obtained at an operating velocity of 0.3 m/s. A 12.7 mm thick Plexiglas flat plate 2.5 m long and 0.85 m wide with a 5:1 elliptical leading edge was utilized as a test section. The plate was supported 10 cm above the channel surface by adjustable legs to allow controlled development of a laminar boundary layer and to prevent interference by channel-wall boundary layers.

Injection holes drilled into the hemispheres and two spanwise dye slots in the flat plate were utilized for dye visualization of hairpin vortices and the wake patterns induced near the test-plate surface. A schematic of the test system is shown in figure 1. Half-cylinder dye manifolds, 75 mm in length and 13 mm radius, were fitted beneath the dye slots to assure uniform dye injection. In all dye-slot flow-visualization experiments the dye injection rate $Q$, was kept below the value of $Q = 32l\nu/20$ (where $l$ is the dye-slot length) suggested by Bogard (1982). He observed the injection rate given by the above equation to be the maximum dye injection rate that can be used without introducing disturbances in the wall flow. Injection of different colours of dye through slot 1 (see figure 1), the hemisphere injection holes, and slot 2 allowed visualization and identification of different sections of the wake, the hairpin vortices, and subsequent secondary flow structures.

Hydrogen-bubble visualization was also extensively utilized for flow visualization, with a transverse, horizontal hydrogen-bubble-wire used for top, combined top–side, and combined top–end viewing of the hemisphere wake. A vertical hydrogen-bubble wire was used for side-view visualization. The experimental equipment and techniques are described in greater detail by Acarlar & Smith (1987).

Using the hemisphere protuberances, a stationary, standing vortex would be generated near the leading edge of the hemisphere, forming a stationary horseshoe-shaped structure passing around the hemisphere (see figure 2). To determine whether the standing vortex had an effect on the hairpin-vortex formation, hemispheres were modified to yield half-teardrop bluff bodies. The half teardrops were constructed by

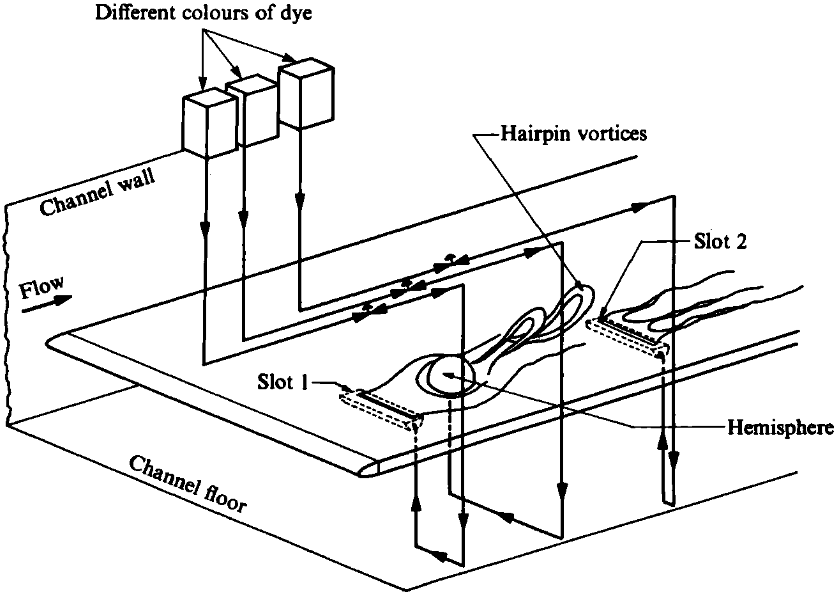

FIGURE 1. Schematic of hairpin generation and dye injection system.

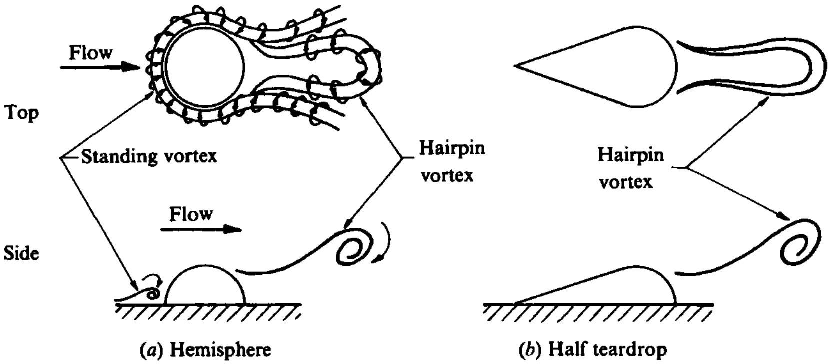

(*a*) Hemisphere (*b*) Half teardrop

FIGURE 2. Comparison of hemisphere and half teardrop.

attaching half-cones to the hemispheres; figure 2 is a schematic of the type of teardrop shape utilized. Using these half-teardrop bodies (with the apex pointing upstream), the standing vortex formed upstream of the hemisphere is eliminated (a side-view of the standing vortex formed with the hemisphere is shown in figure 3). In the absence of the standing vortex, the structure of the hairpin vortices did not appear to noticeably change for the Reynolds-number ranges examined.

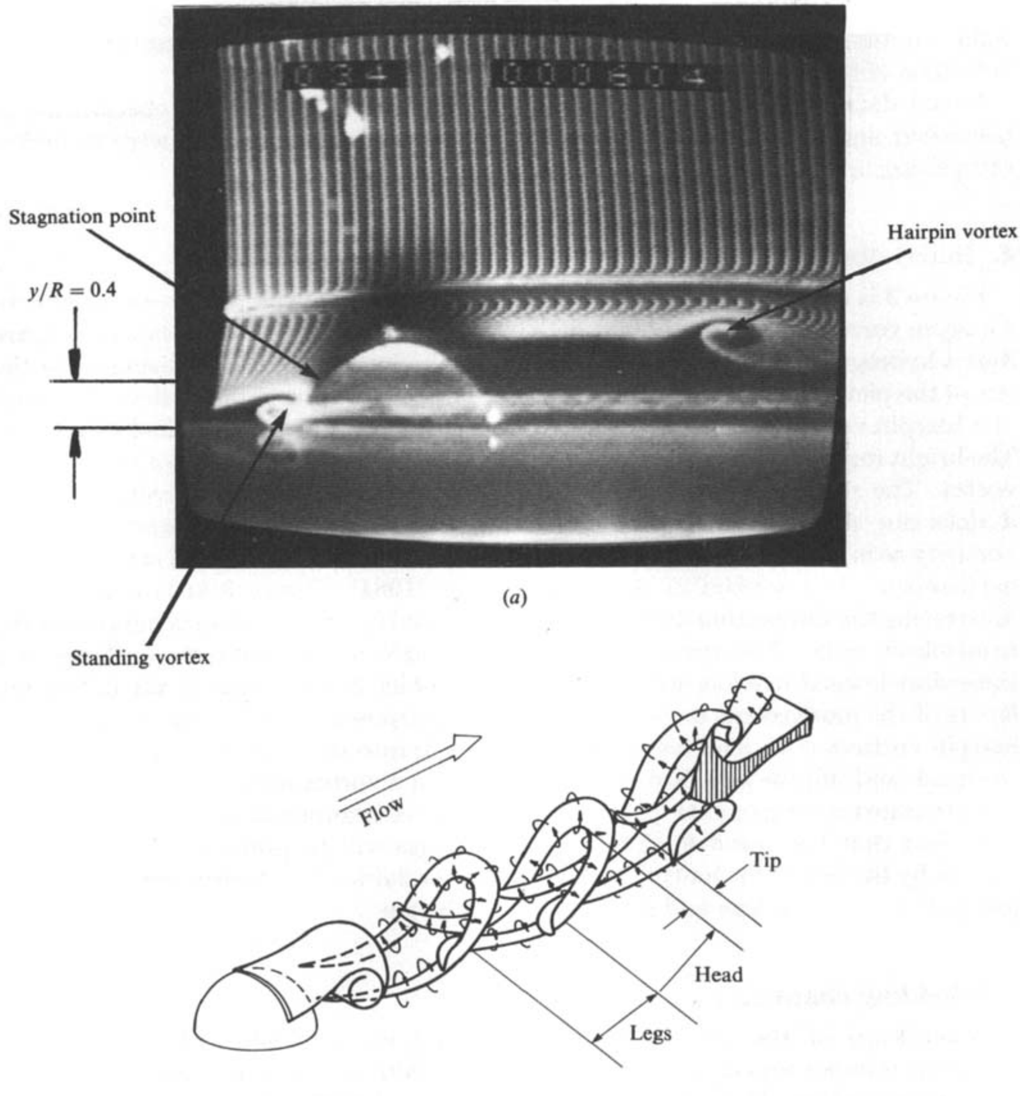

(*a*)

(*b*)

FIGURE 3. Hydrogen-bubble side views: (*a*) general view, (*b*) schematic showing the development and interaction of hairpin vortices created by the three-dimensional separation of the flow over a hemisphere.

## 3. Scope of experiments

Shedding characteristics of the hemispheres were determined using hot-film anemometry and the data acquisition system. In order to cover a broad range of Strouhal number versus Reynolds number (based on hemisphere radius), seven different hemisphere radii (from 3 to 18 mm) and eleven different free-stream velocities (from 3 to 30 cm/s) were examined. To study the additional effect of boundary-layer thickness on shedding frequency, each hemisphere tested was examined at four different downstream locations (35, 43, 67 and 140 cm from the leading edge of the plate). Frequency measurements were done for approximately 352 different cases.

Mean and fluctuating components of the streamwise velocity were measured in the wake on the plane of symmetry at four downstream locations and free-stream velocities of 8 and 15 cm/s.

Visual data includes video sequences taken for both qualitative observation of behaviour and for quantitative evaluation. Six hours of video-tape were recorded, comprising approximately 600 visualization sequences.

## 4. Initial observations

Figure 3 is a side-view hydrogen-bubble visualization of the transverse portion of a hairpin vortex shed from a hemisphere placed in a laminar boundary layer. In figure 3(*a*) a hydrogen-bubble wire is oriented vertically in front of the hemisphere (at the left of the picture) with the bubble lines passing left-to-right with the flow. The head of a hairpin vortex is observed in the bubble pattern to the right of the hemisphere. The bright region upstream of the hemisphere is the transverse portion of the standing vortex. The standing vortex differs fundamentally from the hairpin vortex in that it does not shed periodically. There is no periodic concentration and release of vorticity as in the case of discrete hairpin roll-ups. Details of the vortex concentration mechanism are described in Acarlar & Smith (1984). Figure 3(*b*) is a schematic illustrating the interaction and nesting of sequential hairpin vortices generated in the hemisphere wake. The streamwise legs of multiple loops appear to coalesce in a three-dimensional fashion, with the legs of the older loops caught in the deforming layers of the more recent ones. For descriptive purposes, the structure of individual hairpin vortices is divided (as shown in figure 3*b*) into three sections: (i) the tip, (ii) the head, and (iii) the legs. Note that the 'head' of a vortex contains both transverse and streamwise components of vorticity. For the configuration shown in figure 3(*b*), it is clear that low-speed fluid inboard of the legs will be pumped away from the surface by the legs of the hairpin vortices, whereas fluid will move towards the surface just outboard of the legs and downstream of the tip.

## 5. Shedding characteristics

Dependence of the shedding frequencies and characteristics of the wake on Reynolds number was established using the hot-film anemometry and digital data acquisition system. The periodicity of the vortex shedding from hemispheres was examined over a Reynolds-number range of $30 \leqslant Re_R \leqslant 3400$. For each $Re_R$ case examined, the downstream location and height of the hot-film probe was adjusted such that the maximum amplitude of the fluctuating component of the velocity signal was obtained. Dye visualization was carried out simultaneously to assure that the frequency measured was due to the shedding of individual hairpins. In certain cases, it was realized, by comparison of the dye visualization and the velocity signal, that if the hot-film sensor was located close to the wall both the passage of the head and legs would be sensed by the hot-film probe, resulting in the incorrect interpretation of the shedding frequencies. Employing the dye-velocity signal comparison, downstream location and height of the sensor were optimized such that only the passage of the head was sensed.

Hot-film data was input to the digital data acquisition system and stored on disk. Shedding frequencies were then determined from power-spectral analyses using standard fast Fourier transform techniques on the stored data sets. Shedding frequencies were also cross-checked using an oscilloscope display of the hot-film signal.

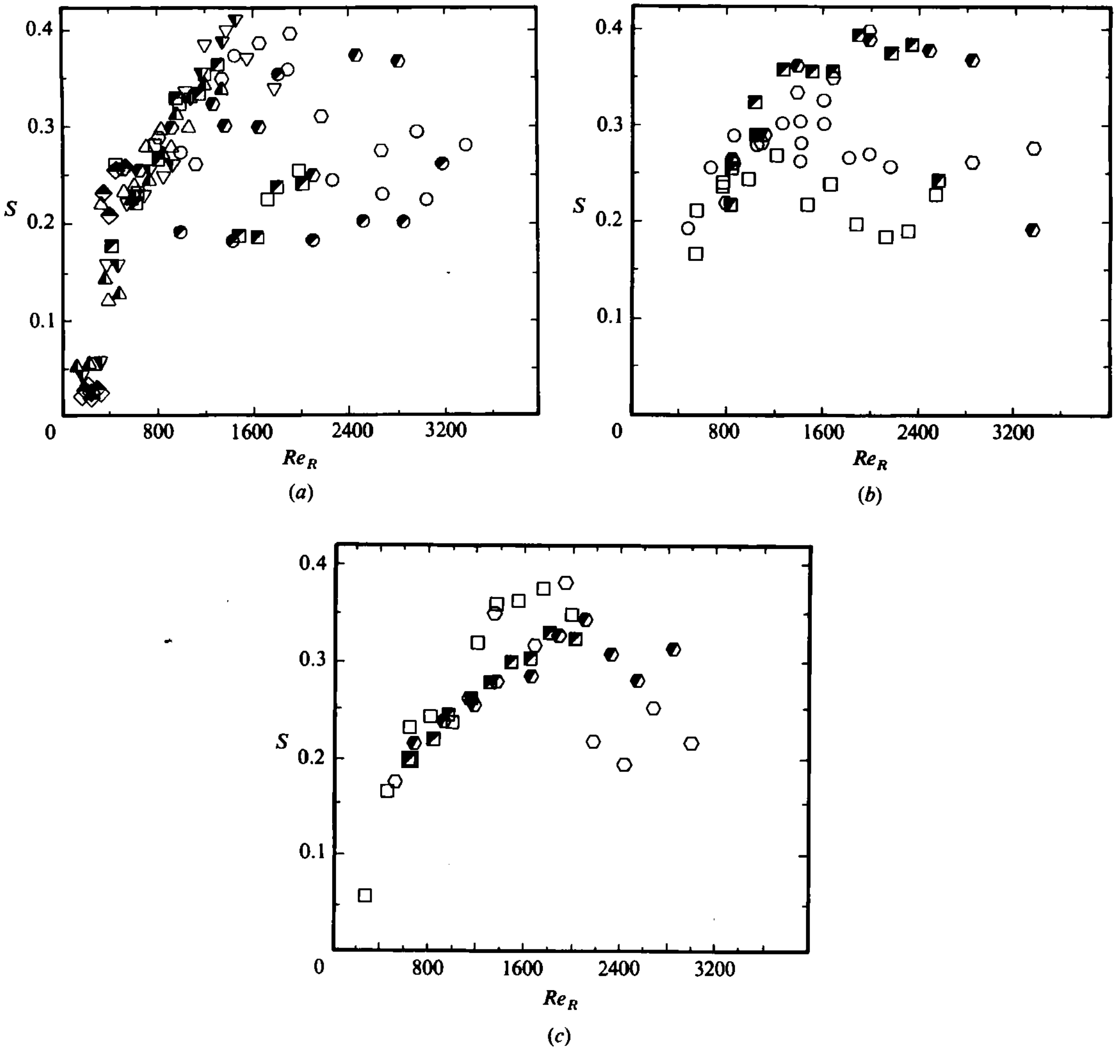

FIGURE 4. Strouhal versus Reynolds number for hemispheres and half teardrops. $S = fR/u$, $Re_R = uR/\nu$ ($u \equiv$ tip velocity; $R \equiv$ radius of hemisphere). (*a*) Hemispheres. Open and half-filled symbols correspond to hemispheres located 140 cm and 35 cm downstream of the leading edge respectively. ◇, $R = 3$ mm; △, 6 mm; ▽, 7 mm; □, 8 mm; ⬡, 12 mm; ○, 18 mm. (*b*) Hemispheres. Open and half-filled symbols correspond to hemispheres 67 cm and 43 cm downstream of the leading edge respectively. ○, $R = 8$ mm; □, 9 mm; ⬡, 12 mm. (*c*) Half teardrops. Open and half-filled symbols correspond to teardrops 140 and 35 cm downstream of the leading edge respectively. □, $R = 8$ mm; ⬡, 12 mm.

It was determined that regular shedding (in the form of distinct hairpins) from hemispheres is initiated at $Re_R \approx 120$, with the wake becoming irregular at approximately $Re_R = 3400$. Since the hemispheres were located in a developing laminar boundary layer, the Reynolds number ($Re_R = uR/\nu$) used to characterize the shedding was based on the velocity within the impinging boundary layer that would exist at the same height as the upper tip of the hemisphere.

Figure 4 shows the Strouhal number (based on the shedding frequency, hemisphere radius and tip velocity) versus Reynolds number. To cover a broad range of $S$ versus $Re_R$, seven different hemispheres from 3 to 18 mm and eleven different free-stream velocity from 3 to 30 cm/s were examined. Figure 4 (*a*) is the result for six different hemispheres and eleven different free-stream velocities. Each experimental point in figure 4 (*a*) represents the mean value of three independent data samples. The range of displacement thickness $\delta^*$ for the different free-stream velocities and two different downstream locations ranged from 1.8 to 10.5 mm; boundary-layer thicknesses varied from 5 to 30.6 mm. From the plot it appears that essentially the same $S$ versus $Re_R$ behaviour occurs at both of the different downstream locations, with the shedding characteristics appearing to scale primarily on tip velocity. The effect of the boundary-layer velocity gradient on the behaviour of the shed vortices (their evolution after the roll-up process) will be discussed in subsequent sections.

Figure 4 (*b*) shows the results for three hemispheres of 8, 9 and 12 mm located at 43 and 67 cm downstream of the leading edge. Within the uncertainity of the experiments the shedding characteristics appear essentially the same as in figure 4 (*a*).

Figure 4 (*c*) shows $S$ versus $Re_R$ determined for the half-teardrops. Comparing figure 4 (*a–c*) it appears that for the same $Re_R$ the half-teardrops yield a slightly lower $S$-value. This is believed to be due to the absence of the standing vortex. It is speculated that the presence of the standing vortex further destabilizes the separating boundary layer over the hemisphere, resulting in higher shedding frequencies. Note that in figure 4 (*a–b*) the $S$-values spread between 0.2 and 0.37 above $Re_R > 1400$. It was observed that for $Re_R > 1400$, the shedding may become unstable with power spectra yielding multiple peaks. The experimental points shown in figure 4(*a*, *b*) above $Re_R \approx 1400$ are the first harmonics of the power spectra with multiple peaks. It is believed that the spreading of the $S$-values between 0.2 and 0.37 is not due to experimental uncertainties but to the physics of the phenomena, since Möller (1938) observed that there are two modes of shedding behaviour for spheres towed in still water. Furthermore, at higher $Re_R$ there may be parameters other than tip velocity and hemisphere radius that affect the shedding frequency.

## 6. Flow patterns

This section presents and interprets a series of single- and dual-view pictures and picture sequences of the periodic hairpin-vortex structures generated in the hemisphere wake. There are two main reasons for examining the flow patterns in detail. The first is a lack of understanding of how such three-dimensional vortex structures behave and interact both with each other and with the boundary surface. Therefore, an examination of these patterns should provide an understanding of the development/interaction process. The second is to examine the suggestion of previous studies that these loop structures are a sustaining structure of turbulent boundary layers. Examination of this latter suggestion will be done by comparison of the patterns generated by the hairpin vortices with those commonly observed in the near-wall region of a turbulent boundary layer.

The pictures presented in this section are of dye and hydrogen-bubble time-line patterns obtained in the hemisphere wake with the bubble wire at different locations both downstream from the hemisphere and above the wall (see figure 5 for characterization). The intent is to illustrate the variations in the flow patterns that are observed in the hemisphere wake and to use these to interpret the actual flow behaviour at different cross-sections. This information is used to illustrate the intricate dynamics of the development and interaction of the hairpin vortices.

The wake of a hemisphere can be divided into three regions based on the

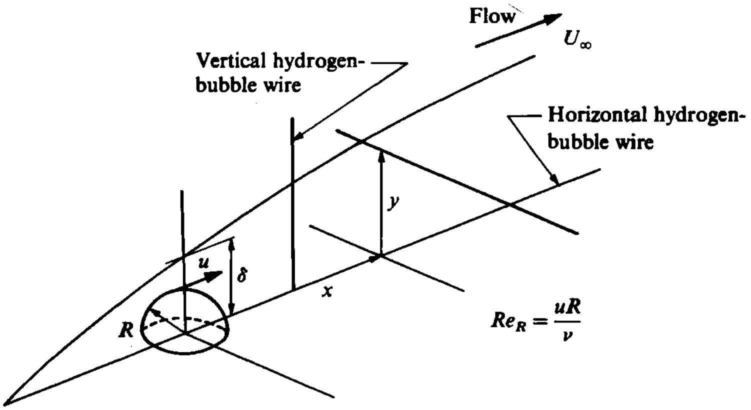

FIGURE 5. Schematic showing the orientation of the hemisphere and the hydrogen-bubble wires in an initially laminar boundary layer.

behavioural characteristics of the structures. There are: (i) a near-wake region, which is the zone immediately downstream of the hemisphere where hairpin-vortex formation takes place; (ii) a zone immediately following the near-wake region where the evolution and growth of the hairpin vortices take place; (iii) a far-wake region, where secondary structures generated owing to the presence of the hairpin vortices interact with the original hairpins, initiating chaotic behaviour. The downstream location of each region is observed to be Reynolds-number dependent. Increasing the Reynolds number causes the regions to approach the hemisphere. For the Reynolds-number range examined, the downstream location of each zone was observed to be approximately: near-wake region 0–3 $R$; growth region 3–15 $R$; and far-wake region 15–80 $R$. Details of each region will be fully examined in the following sections.

### 6.1. *Near-wake structures*

Boundary-layer flows (laminar or turbulent) can be characterized as a shear layer adjacent to a surface. This shear layer can be represented by vortex sheets made up of vortex lines (Utami & Ueno 1979). If a part of this layer is deformed slightly owing to a disturbance (e.g. pressure fluctuations, solid protuberances, etc.), vortex lines can concentrate to form a visible vortex core.

The same concept of concentration of vorticity can be used to describe the formation of the standing vortex and the hairpin vortices which form in the vicinity of a hemisphere protuberance. Initially, as the laminar boundary layer impinges upon a hemisphere, the undisturbed vortex sheets laying below the upstream stagnation point (shown in figure 3$a$) undergo a retardation. The impinging vortex sheets roll-up to form a standing vortex, as shown schematically in figure 6.

The mechanism of formation of hairpin vortices is different to the formation of the standing vortex. The mechanism is a process of build-up and release of concentrated vorticity in which the base pressure (a low-pressure region downstream of the hemisphere) plays a major role. Once the boundary layer separates from the body, it drags fluid downstream with it. The outer flow field begins to narrow the region between the separated boundary layer and the wall causing the streamlines to curve inwards. In order to balance the pressure across the curved streamlines, a centrifugal force field develops owing to the inward-spiralling motion of the outer flow (Wille 1972). It is this reaction to the curvature of the outer irrotational flow field which

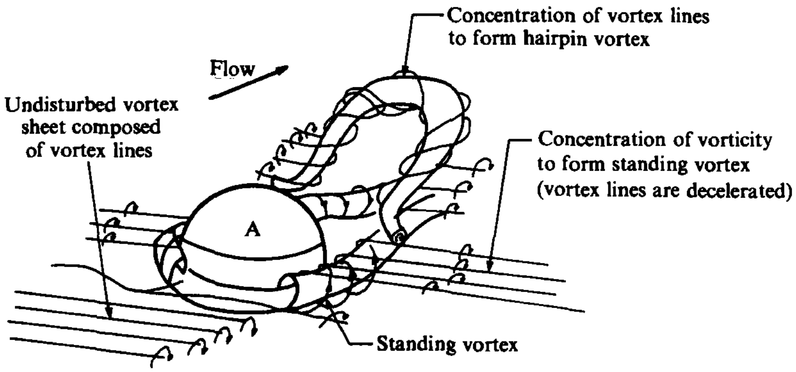

FIGURE 6. Formation of hairpin vortices and standing vortex due to concentration of vortex lines.

causes the vortex lines to concentrate and form the hairpin vortices. The separated boundary layer and the spiralling motion play the role of the disturbance that causes the concentration of vorticity.

Thus, the main mechanism of the vortex formation is the reaction of the potential flow to the base pressure. The vortex lines spiral inwards as a reaction to this low-pressure region and concentrate to form a vortex tube (figure 6). Once vorticity is concentrated, it is discharged to the main flow as discrete hairpin vortices. After one hairpin vortex has been discharged, a subsequent hairpin immediately begins to develop. Figure 7 is a schematic of the appearance of the near-wake flow structure generated by the shedding hemisphere. The schematic is deduced from the top- and end-view hydrogen-bubble-visualization pictures described below. The hairpin-vortex formation process is described in further detail in Acarlar & Smith (1984).

Figure 8 is an end view of the formation of the hairpin and standing vortex. Placing the wire upstream of the hemisphere allows the direct visualization of the standing vortex. The flow-visualization technique is described in §6.3.

To illustrate the dynamics of the vortex formation in the near-wake, a time sequence of a top–end-view hydrogen-bubble visualization of the developing wake flow is shown in figure 9. These combined-view pictures are obtained using a separate video camera for each view; the two views have been superposed using a split-screen capability of the video system. The initial picture in this sequence (figure 9*a*) is a view at the instant the bubble wire is turned on. Note that both the top and end views are identically aligned and magnified. At $t^* = t/T = 1.8$ (where $t \equiv$ time, $T \equiv$ period of shedding), the initial bubble lines are observed in end view to move vertically between the counter-rotating legs of the hairpin (marked as A). The kinks observed in the top view, marked B, are the low-speed lift-ups caused by the standing vortex. Figure 9(*c*), taken at $t^* = 3.37$, shows the lifted-up bubble lines wrapping around the counter-rotating legs of the hairpin vortex (marked as C). Portions of the bubble lines rotating with and around the legs are observed to move upstream under the influence of (i) the back pressure and (ii) a local streamwise pressure gradient generated along the axis of the counter-rotating legs because of non-uniform vortex stretching. At $t^* = 4.50$, figure 9(*d*), bubble lines observed in region A curl outward, beginning to concentate around the legs. Figure 9(*e*), $t^* = 7.30$, clearly shows the cores of the legs of the hairpin vortex (the dark circles of unmarked fluid in the lifted bubble concentrations) as well as two symmetric upwellings to either side of the hemisphere, B. Figure 9(*f*) is an expanded top view, identical with that shown in

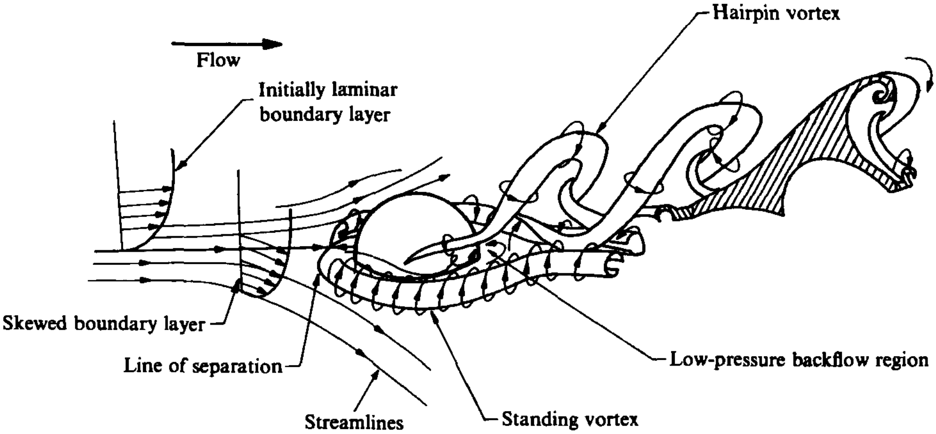

FIGURE 7. Schematic of near-wake structures in the hemisphere wake. Arrows indicate direction of flow or rotation.

figure 9(*d*), which clearly illustrates both the backflow along the hairpin legs and the extent of the kinked low-speed regions created by the lift-up effect of the standing vortex.

Figure 10(*a*) is a top-view bubble-wire visualization within the low-pressure separated region just downstream of the hemisphere, obtained with the bubble wire located at $x/R = 3$ and $y/R = 0.367$. When the bubble wire is initially turned on, hydrogen bubbles that are caught in the cores of the counter-rotating legs display a swirling motion which reveals the legs of the hairpin marked as A. The low-pressure separation region upstream of the bubble wire causes the swirling bubble concentrations to move rearward in the opposite direction to the mean flow. These bubbles then move to the sides where they are entrained by fluid which causes them to reverse their rearward movement; the bubbles then move downstream and toward the surface, curling inward and around the legs of the hairpin before moving downstream out of the field of view.

A schematic illustrating the inrush of the outer flow and the generation of the hairpin vortices is given in figure 11. A fluid particle approaching the hemisphere from upstream at a height above approximately $y/R = 0.4$ (labelled as A) will not be entrained into the standing vortex, but will pass into the hairpin formation zone where it will orbit around the core of the counter-rotating legs and be carried away by the hairpin vortex. The downstream position of this fluid particle is labelled as A′. A particle, labelled B, which is originally upstream of the hemisphere, but below a height of $y/R = 0.4$, will be entrained by the standing vortex. This particle will then be discharged through the downstream extensions of the standing vortex. The downstream position of this particle is labelled as B′ in figure 11.

### 6.2 *Evolution and development of the hairpin vortices*

In order to follow the development and evolution of hairpin vortices, they were visualized from a Lagrangian reference frame utilizing a traversing platform. A side camera was mounted on the traversing platform and the velocity of the platform was matched with the convection velocity of the heads of the hairpin vortices. Figure 12 is a dye visualization of the evolution and development of the hairpin vortex as observed from a Lagrangian reference frame. In this series of pictures, dye is

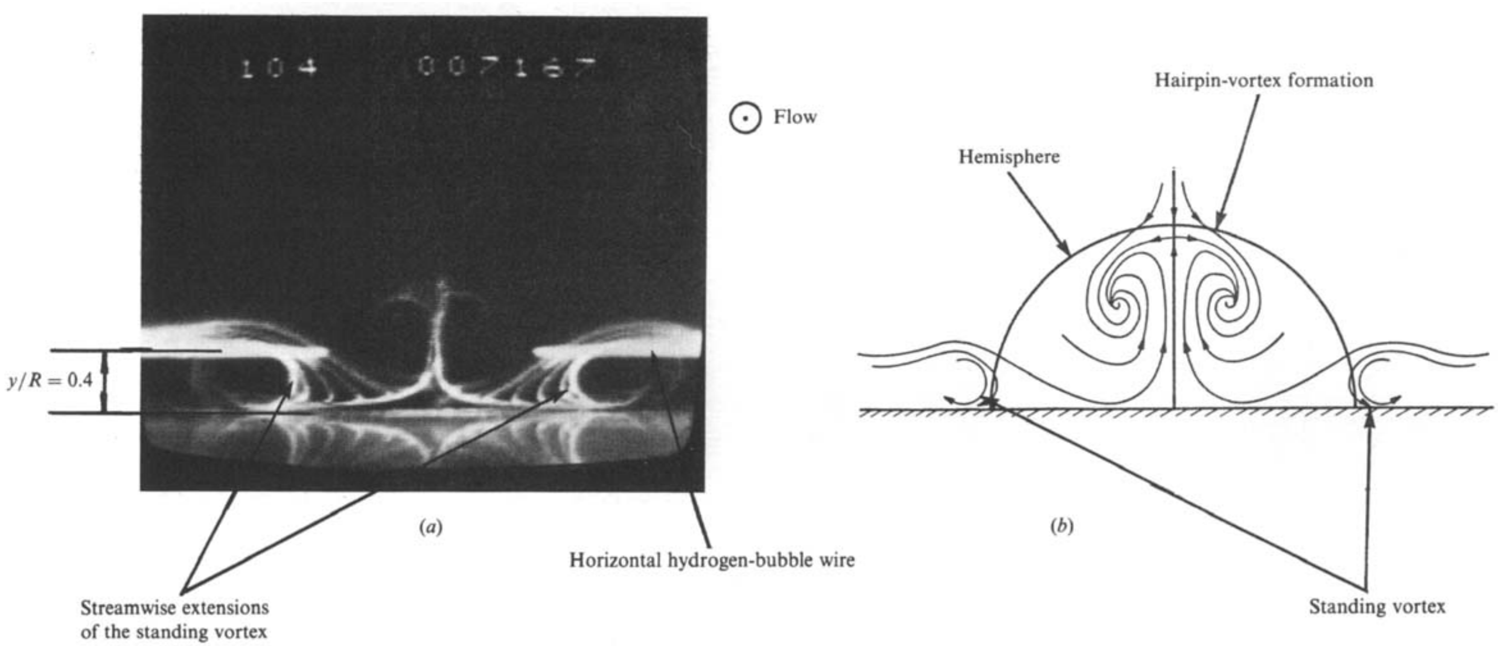

FIGURE 8. End view of vortex formation. Bubble wire located upstream of the hemisphere at $x/R = -1.8$. (*b*) is a schematic of the bubble-wire visualization (*a*).

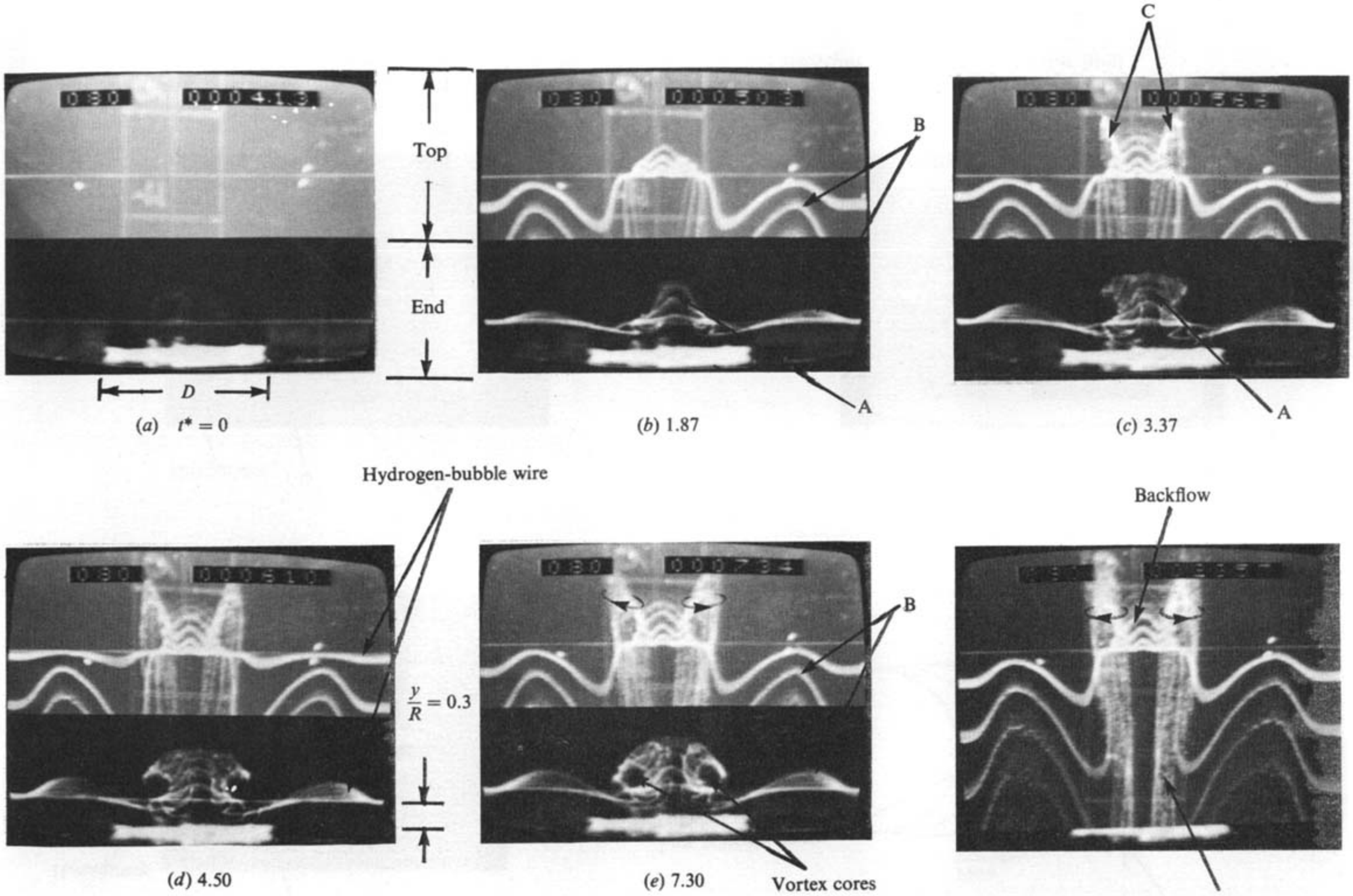

(*a*) $t^* = 0$ (*b*) 1.87 (*c*) 3.37

(*d*) 4.50 (*e*) 7.30 (*f*) 7.30 (expanded topview)

Figure 9. Time-sequence visualization of vortex formation in the near-wake. $Re_R = 800$, $x/R = 3$, $t^* = r/T$ ($t \equiv$ time; $T \equiv$ period of shedding).

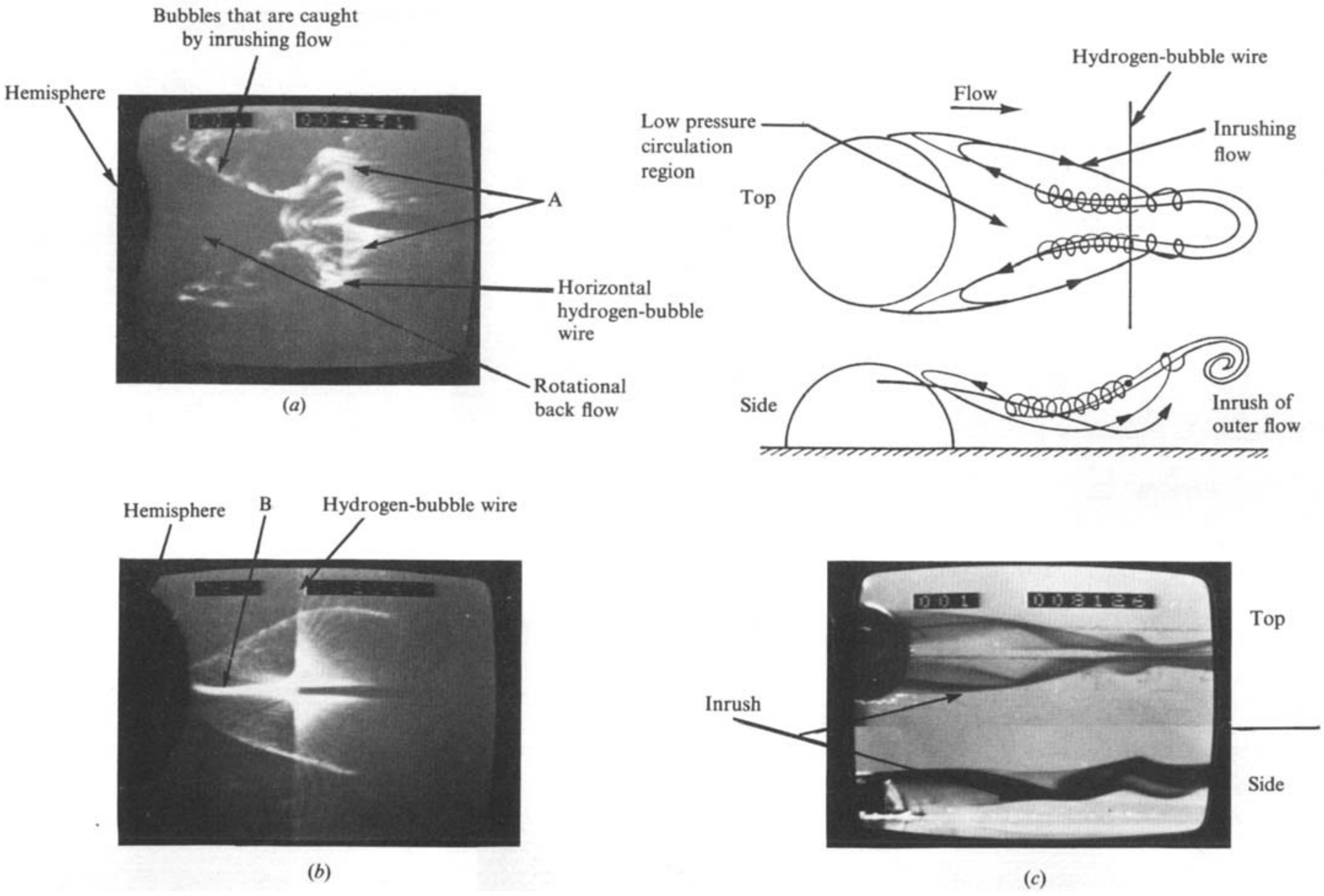

FIGURE 10. Near-wake flow patterns. (*a*) Top view hydrogen-bubble visualization and schematic $y/R = 0.367$; $x/R = 3$; (*b*) top view $y/R = 0.05$, $x/R = 2$; (*c*) top–side dye visualization of the inrush of outer fluid.

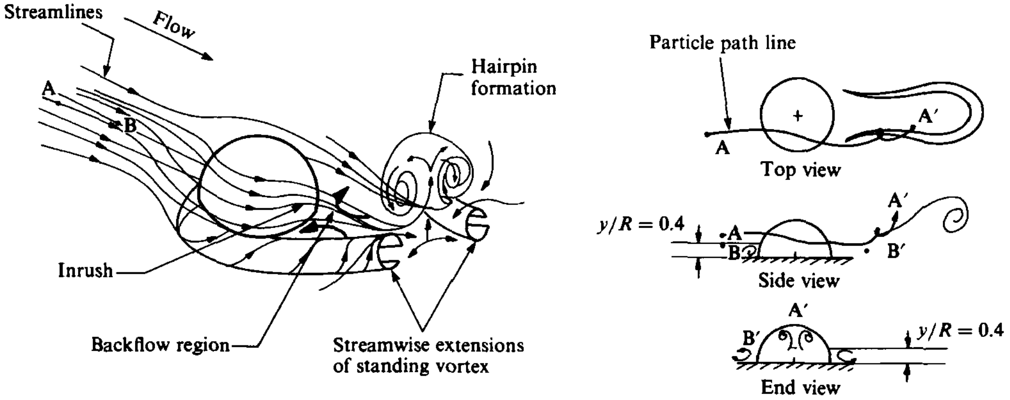

FIGURE 11. Schematic of inrush of outer flow and formation of hairpin vortices.

introduced into the wake through holes on the hemisphere. Figure 12(*a*) is the dye pattern at $x/R = 5$ produced by two sequentially generated hairpins. This figure clearly demonstrates the three-dimensional nesting of the hairpins as the counter-rotating legs of vortex A intertwine with the head of a younger vortex B. Figure 12(*b*) shows the effect of stretching by the local velocity gradient on the evolution of hairpin vortices. Note that a portion of the counter-rotating legs (marked AA′ starts to flatten (i.e. rotate in a clockwise direction), making a shallower angle with the wall. It is observed that AA′ is a portion of the legs that moves together owing to image-vortex effects. It is believed that as this portion of the legs moves together, the vorticity contained within the legs in this region will undergo a viscous interaction with each other, resulting in the reduction of vorticity concentrated in each of the cores due to mutual cancellation. Since the induced upward velocity of the legs will be reduced owing to a decrease in vorticity, the mean shear flow will cause these weakened portions of the legs to rotate towards the wall, forming region AA′. This effect will be fully examined in § 8.1.

At a downstream location of $x/R = 10$, figure 12(*c*), the portion AA′ of the counter-rotating legs has become essentially parallel to the wall. Figures 12(*d*) further illustrates the diffusion and weakening of region AA′ and the diffusion of the vortex head. Once the head of the hairpin vortex is out of the shear layer (boundary layer), as shown in figure 12(*e*), the rotational effect of the mean shear gradient ceases to oppose the induced velocity of the head, which results in the head curling backward into the free stream. The counter-rotating legs that remain in close proximity of the wall maintain their integrity and coherence owing to stretching.

### 6.3 *Structure of the hairpin vortex*

*Top Views* The three-dimensional structure of the hairpin vortex was studied at a series of downstream locations utilizing a horizontal hydrogen-bubble wire. At each location, top views were recorded for a series of bubble-wire heights above the surface. Figure 13 illustrates the effect of bubble-wire height on the bubble time-line patterns obtained at a downstream location of $x/R = 6$. One should keep in mind that the visible patterns are not the structures themselves, but their 'footprints', i.e. the effects of the hairpin-vortex structures on the fluid sheets which are marked by the hydrogen bubbles. It is clear that flow patterns observed in the near-wall region vary widely in appearance. Although this is due in part to the complex nature of the flow, careful studies showed that small changes in the location of the bubble wire, the phase

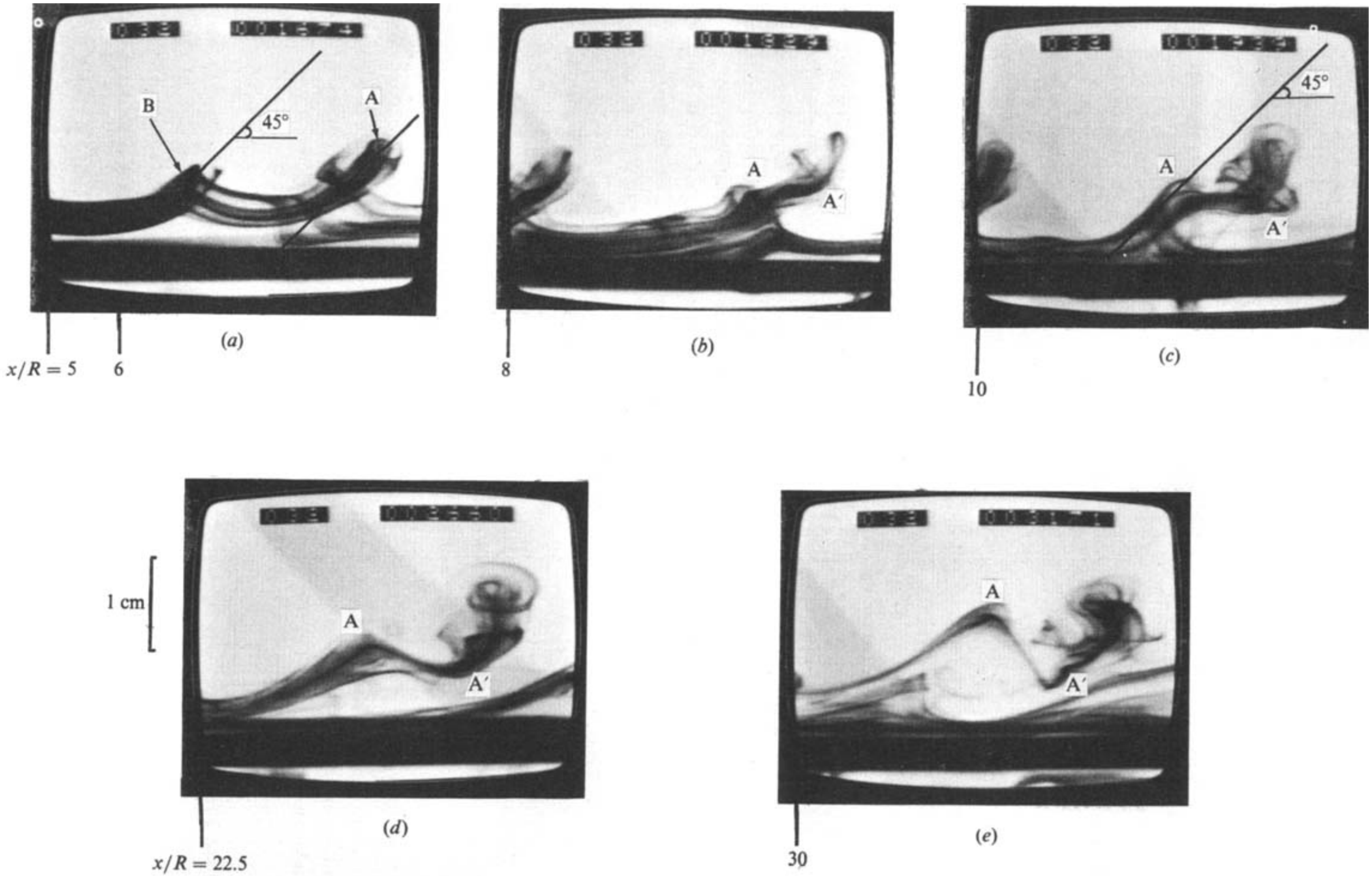

(a) (b) (c) (d) (e)

FIGURE 12. Evolution of a hairpin vortex of various downstream locations; $Re_R = 810$.

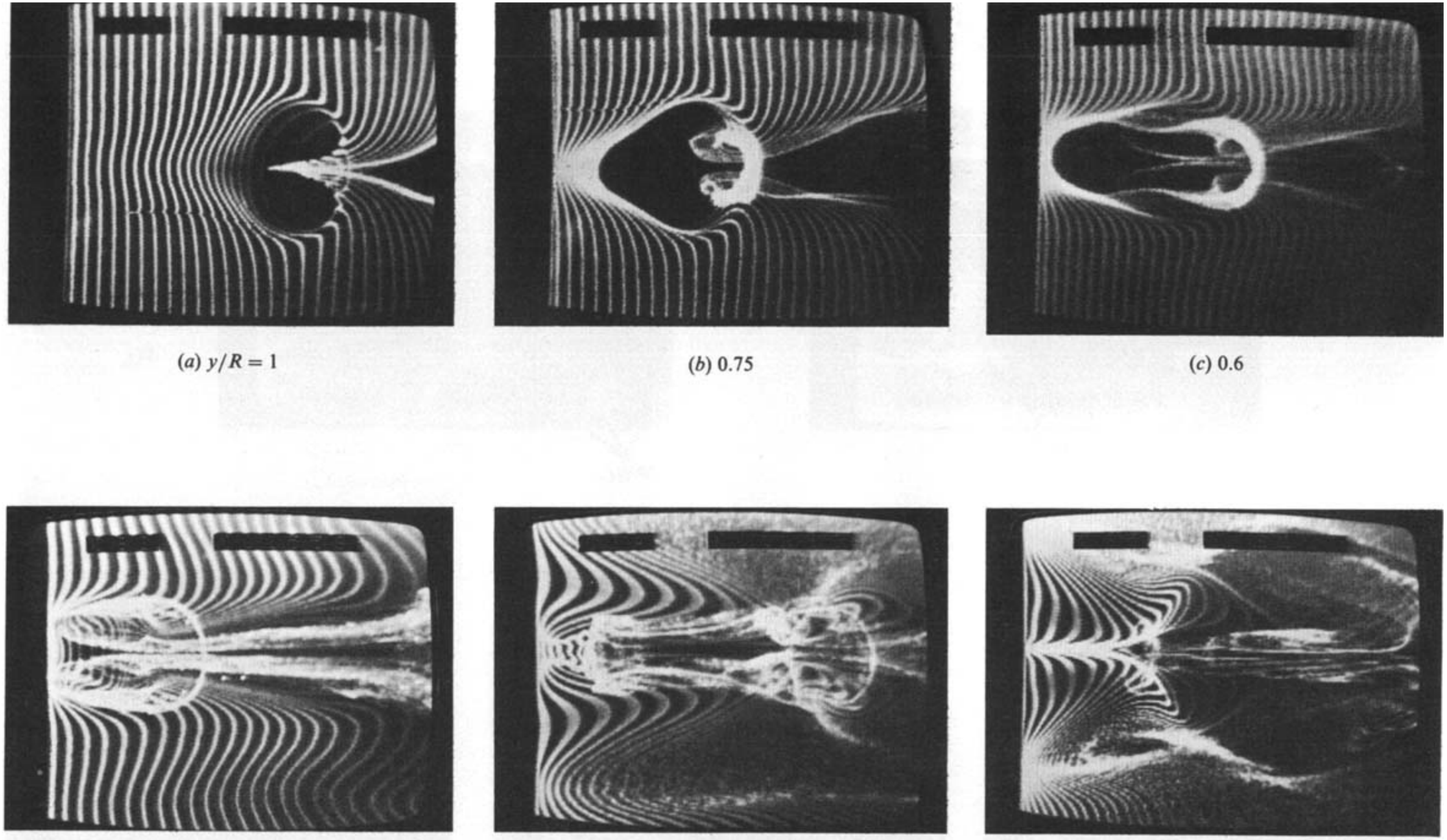

(*a*) $y/R = 1$ (*b*) 0.75 (*c*) 0.6

(*d*) 0.5 (*e*) 0.375 (*f*) 0.25

FIGURE 13. Top views of bubble-line patterns for different bubble-wire heights. Downstream wire location $x/R = 6$. $Re_R = 750$, $\delta/R = 1.2$.

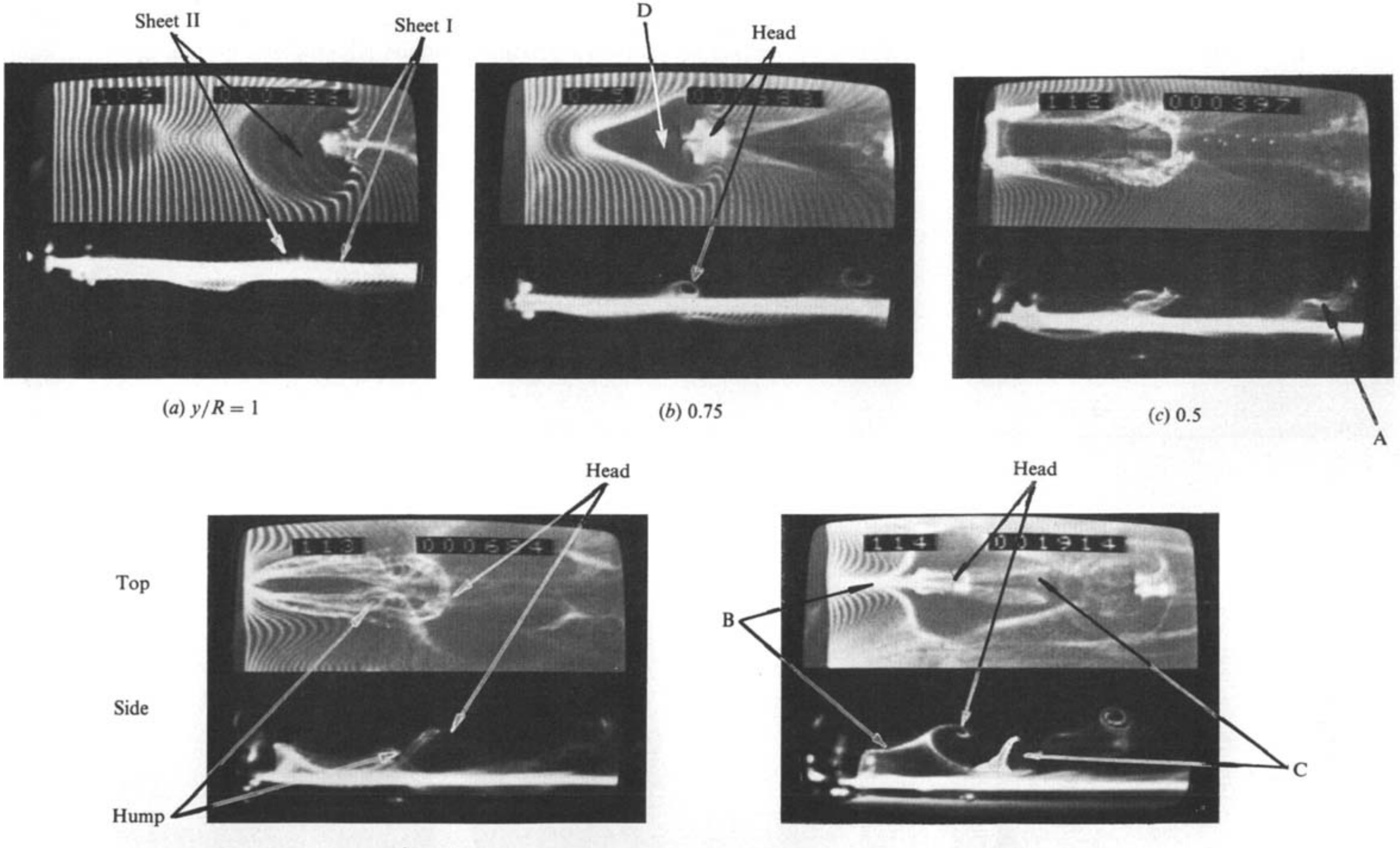

(a) $y/R = 1$ (b) 0.75 (c) 0.5

(d) 0.375 (e) 0.25

FIGURE 14. Combined top–side views at $x/R = 5$ for different wire heights above the wall. $Re_R = 750$, $\delta/R = 1.2$.

of development, or even the frequency of bubble-line generation may have a tremendous effect on the visualized patterns. Unlike dye or smoke, which carry the history of the flow, the bubble-lines reveal only local behaviour; thus when attempting to visualize the evolving three-dimensional flow structures as they are convected downstream, what one will observe is a series of significantly different bubble-line patterns representing the local, active fluid motions induced in a specific region during a particular phase of the structure's development.

In general, figure 13 illustrates the complexity and the substantial interaction between sequential vortex loops, and the dependence of the type of pattern observed upon the location of the bubble wire and the phase of the development. It was found that interpretation of the patterns and the complex three-dimensional motions they represent was often quite difficult owing to an inability to accurately establish motion in or out of the viewing plane. In order to address this issue, the dual-view capability of the video system was utilized. Having access to two views of the three-dimensional structure allowed the three-dimensional flow behaviour to be more accurately established.

*Dual Views* The high-speed video system utilized in this study allows stimultaneous viewing and recording of two separate views using two identical video cameras. The images are simultaneouslly displayed on the viewing screen using a split-screen feature, which proves invaluable in detecting rotational behaviour and visualizing complex three-dimensional interaction of vortices. Without simultaneous access to both the side- and top-view pictures, it is very difficult to understand the complexities of the three-dimensional fluid motion.

Figure 14 is a series of combined side and top views obtained at a downstream location of $x/R = 5$. Examining figure 14, one of the major advantages of dual-view observation is immediately obvious. It is clear that without access to both the side and top views in these pictures it is very difficult to understand the complexity of the fluid motion. In fact, the video sequences from which figure 14 was obtained revealed that many of the previous inferences of the three-dimensional behaviour of hairpin vortices (made with access to only a single view) were incorrect; in several cases the inferred fluid motion was even opposite to the direction assumed.

One of the difficulties of the split-screen viewing technique is the establishment of appropriate lighting to assure acceptable pictures in both the vertical and side directions. In addition, establishing alignment and identical magnification for each of the cameras requires special care. Often total alignment of both pictures is not possible because of the viewing angle required to yield the best visualization pictures. For example, note that there is a slight misalignment of the dual-view flow patterns shown in figure 14 (the side-view patterns appear to lag the top view patterns) since the side camera was intentionally slightly skewed in the horizontal plane to provide a better view.

Each picture in figure 14 was obtained with the horizontal bubble wire at a different height above the surface in order to visualize the various characteristics of the hairpin-vortex structures and the induced behaviour in different regions. Figure 14(*a*) is obtained with the wire at $y/R = 1$, the same height as the single view shown in figure 13(*a*). As the tip of the hairpin vortex impinges on the bubble sheet (the time-streak sheet composed of hydrogen-bubble time lines), bubble lines are deformed and stretched by the rotating loop. For descriptive purposes, the portion of the bubble sheet that is downstream of the vortex tip, and the portion that is upstream of the tip are respectively marked as sheet I and sheet II. In figure 14(*a*), the bubble lines

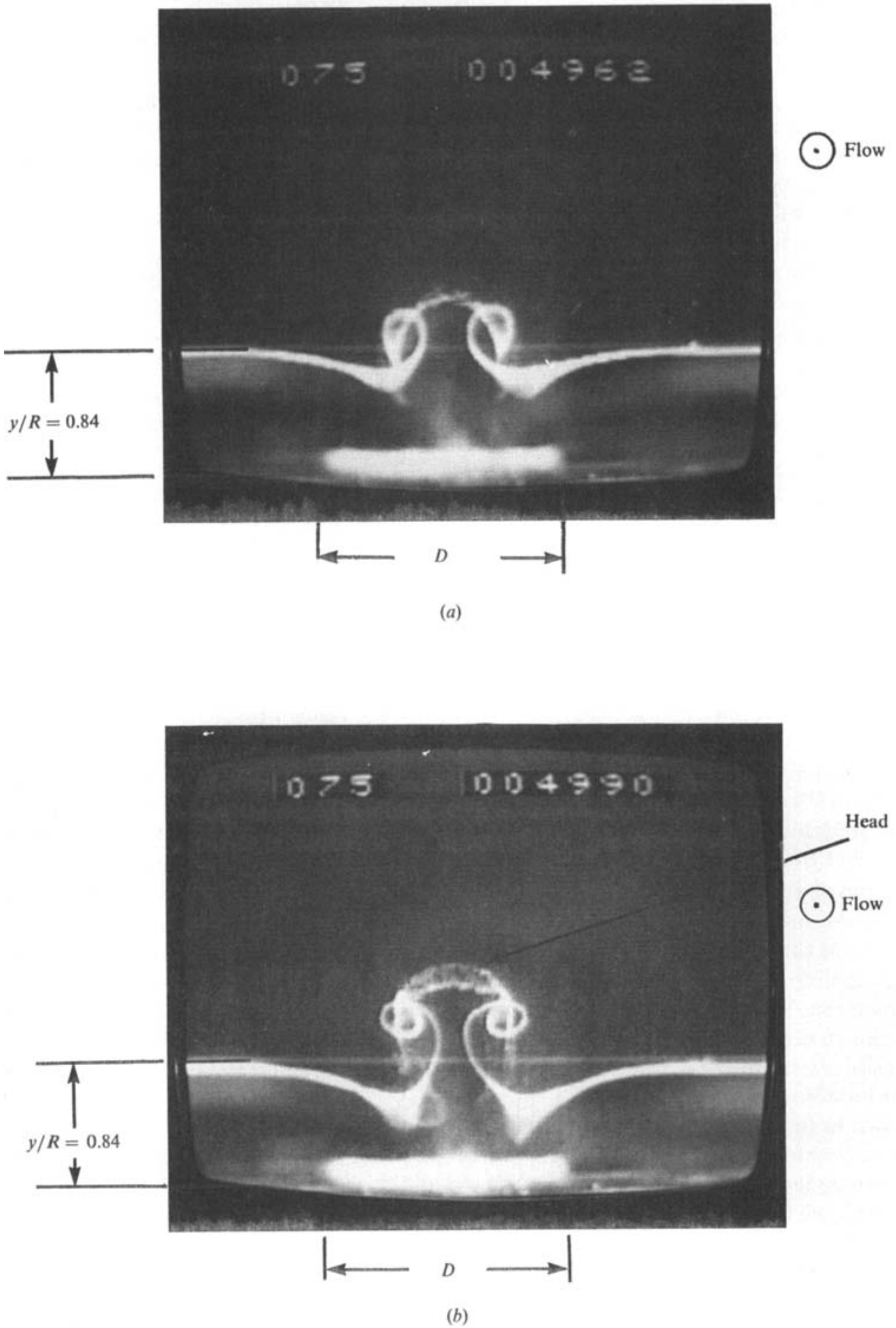

(*a*)

(*b*)

FIGURE 15(*a*,*b*). For caption see facing page.

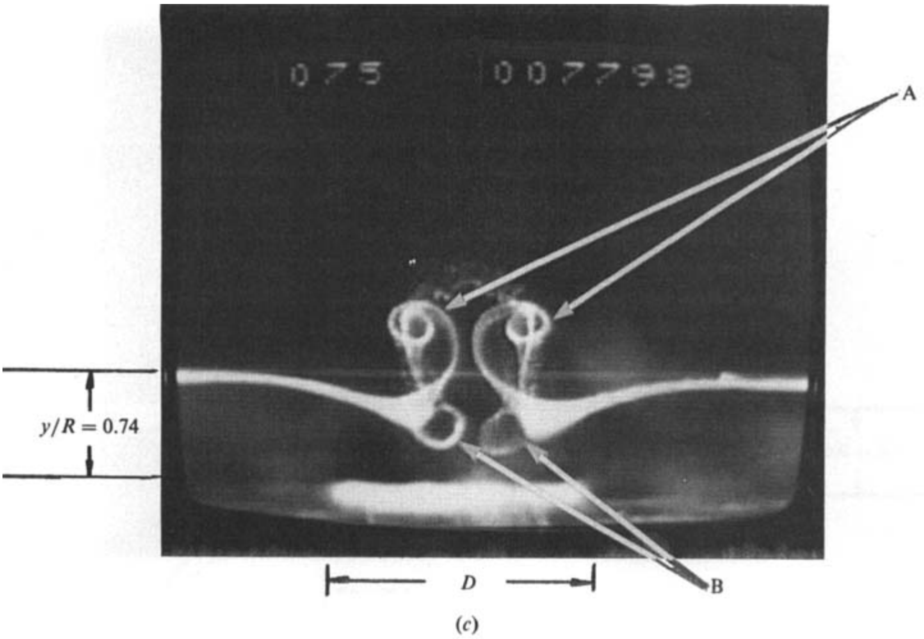

FIGURE 15. End-view of the hairpin vortex at $x/R = 5$. Pictures (*a–c*) are 0.25 s apart.

that form sheet I are retarded, pulled downwards and stretched towards the wall, whereas the bubble lines that comprise sheet II are accelerated forward, pushed upwards (towards the observer out of the plane in figure 14) and stretched. The corresponding vertical motions of these sheets are clearly shown in the side view. At $y/R = 0.75$, figure 14(*b*), the head becomes more apparent, with the bubble-free region (marked as D) appearing just upstream of it. This bubble-free region is caused by the induced flow of two sequential hairpin heads. The bubble lines that were originally in the upstream section of region D have been retarded by the tip of the younger vortex whereas the bubble lines originally in the downstream region of D have been accelerated forward by the head of the older hairpin vortex. These two induced flows essentially 'wash out' the bubble lines that were originally in region D, clearly characterizing a saddle-point behaviour. Note the slight misalignment problem pointed out previously. Also note the similarity of the bubble-free 'heart-shape' patterns in figures 14(*a*, *b*) and 13(*a*, *b*) to the 'pockets' observed by Falco (1981) using smoke visualization.

When the bubble wire is lowered to $y/R = 0.5$ (figures 14*c* and 13*d*) the effect of the legs becomes visible. Note the kink (labelled A in figure 14*c*) that is created as a result of the mutual cancellation effects of the migrated-together portions of the counter-rotating legs. Figure 14(*d*) (see also 13*e*), with the wire located at $y/R = 0.375$, shows the bubbles collected into the tip, head and legs of the loop, providing a clear indication of the shape of the hairpin and its inclination to the surface. The 'hump' in figure 14(*d*) is formed owing to the coalescence of the upstream portions of the legs of the older hairpin with the head of the younger hairpin. From the slow-motion review of the original video sequences, it appears that this pairing process results in a sudden increase in the streamwise component of the vorticity of the head. This streamwise coalescence appeared to precipitate the sudden movement of the hairpin upward and downstream due to increased mutual induction effects.

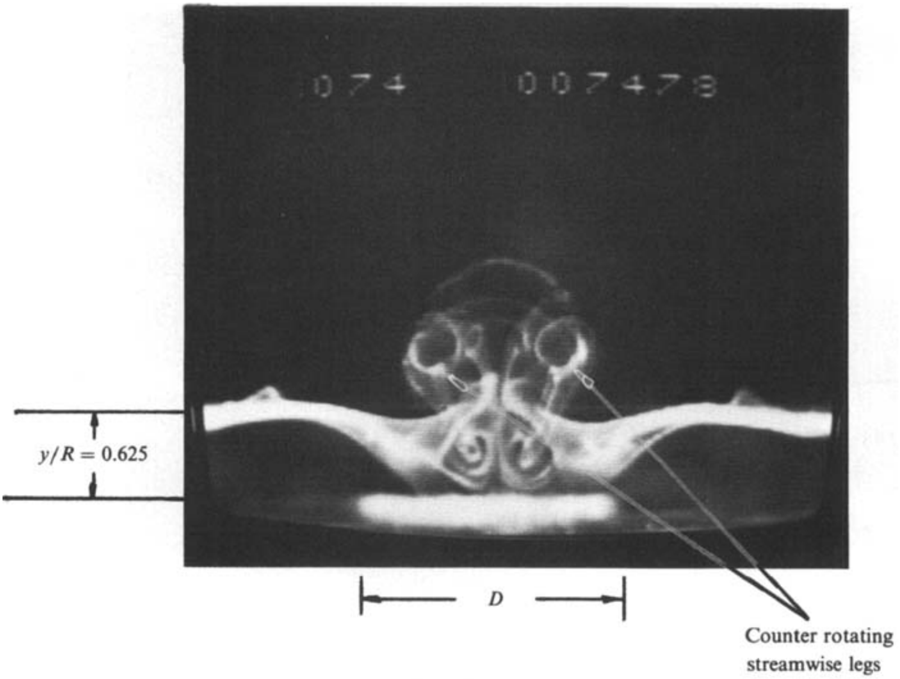

FIGURE 16. End-view visualization of counter-rotating streamwise legs. $Re_R = 800$, $x/R = 5$.

It has been observed that this coalescence process also occurs near the wall between the stretched legs of the two sequential hairpin vortices.

Lowering the bubble wire further to $y/R = 0.25$ yields the flow patterns shown in figure 14(*d*) (also 13*f*). Formation B is the low-speed ridge of fluid lifted up from the surface by the streamwise sections of the head of the hairpin vortex. Careful studies of slow-motion video sequences showed that bubble formation C is a very rapid eruption of fluid from the wall region caused by the counter-rotating legs.

From the above visualization studies, it has been observed that the legs and heads of multiple hairpins appear to coalesce in a three-dimensional fashion as the individual hairpins undergo a complex stretching process. In order to determine the relative size of the counter-rotating legs of the hairpins and to further illustrate three-dimensional behaviour of hairpins, a series of end-view visualization studies were carried out.

*End Views* End views of the generation and evolution of hairpin vortices were visualized using a horizontal (spanwise) hydrogen-bubble wire. Use of dye visualization proved unsatisfactory due to the dark background experienced when looking upstream from the end view. A front-silvered wedge mirror (to assure the symmetry of the flow field) was located 30 cm downstream of the hairpin generation location to avoid upstream effects of the mirror on hairpin generation. The apex angle of the mirror was optimized at 30°, which was found to minimize blockage effects while providing a sufficient reflection angle. To assure that the flow is not affected by the presence of the mirror, the flow field was visualized at a series of locations upstream of the mirror to examine qualitative changes; it was established that the mirror imparts no changes in the regions of interest.

Figure 15 illustrates the passage of the head of a hairpin vortex through the bubble-generation plane. The frequency of bubble generation was synchronized with the frequency of vortex shedding such that a single vortex is marked by a single hydrogen-bubble line. As the head of a hairpin vortex passes through the single bubble line, bubbles that are between the counter-rotating legs move upward, whereas bubbles just outboard of the legs move towards the wall. Figure 15(*a*, *b*) clearly demonstrates both the rotation of the bubble line around the head and the legs of the hairpin vortex and the movement of the head and legs away from the surface. Lowering the wire to $y/R = 0.74$ allowed the visualization of a longer portion of the streamwise counter-rotating legs, as shown in figure 15(*c*). Comparison of the spanwise distance between the counter-rotating legs at A and B (A is closer to the observer) clearly illustrates that the trailing portions of the legs are closer together.

Figure 16 is obtained at the same downstream location as figure 15, but using a longer-duration (wider) bubble line. Increasing the width of the bubble lines allows the marking of a much broader portion of the hairpin vortex as it passes through the bubble-generation plane. By using this technique, a substantial extent of the counter-rotating legs is visualized.

### 6.4 *The generation of secondary structures*

Further examination of bubble-line flow patterns in the hemisphere wake indicates the development of secondary flow structures in the initially laminar boundary layer due to the presence of the hairpin vortices. Figure 17(*a*), obtained at a downstream location of $x/R = 7.5$ and bubble-wire height of $y/R = 0.638$, illustrates the formation of two bubble-free regions (marked as A) to the sides of the original hairpin. Region B reflects low-momentum fluid lifted up between the counter-rotating legs of the original hairpin. Lowering the wire to $y/R = 0.465$, at the same downstream location, (figure 17*b*) reveals the cause of these two bubble-free, dark regions. These dark regions appear to be related to the formation of secondary hairpin-type structures, as indicated in figure 17(*b*). The formation of these bubble-free pockets is similar to the development of the saddle-point behaviour for the initial hairpin structure, illustrated in figure 14(*b*). The suggested mechanism for formation of these secondary hairpins is illustrated in figure 17(*c*). Low-momentum fluid lifted up from the surface by the standing vortex interacts with the higher-speed outer boundary-layer flow, resulting in the generation of a three-dimensional shear layer which rolls-up to form a secondary hairpin vortex. A similar mechanism is also suggested by Perry, Lim & Teh (1981) to describe the lateral development of a turbulent spot in transitional boundary layers. In the original video sequences, these secondary hairpin vortices appear to exhibit a much lower angular rotation (i.e. vorticity) in comparison with the original hairpin vortices.

In addition to the secondary hairpins generated to the sides of the original hairpin vortex, other secondary vortical structures are generated on the plane of symmetry. Figure 18 illustrates the transverse head of a secondary vortical structure trailing the original hairpin vortex. These secondary vortices are generated owing to the roll-up of a three-dimensional shear layer which is created by the interaction of higher-speed outer boundary-layer flow with the low-momentum fluid lifted-up from the wall by the counter-rotating legs of the original hairpin vortex.

It is believed that the interaction of these secondary vortical structures, generated both at the outer edges of the legs and on the plane of symmetry, is the mechanism that increases the complexity of the flow structure, eventually yielding what is

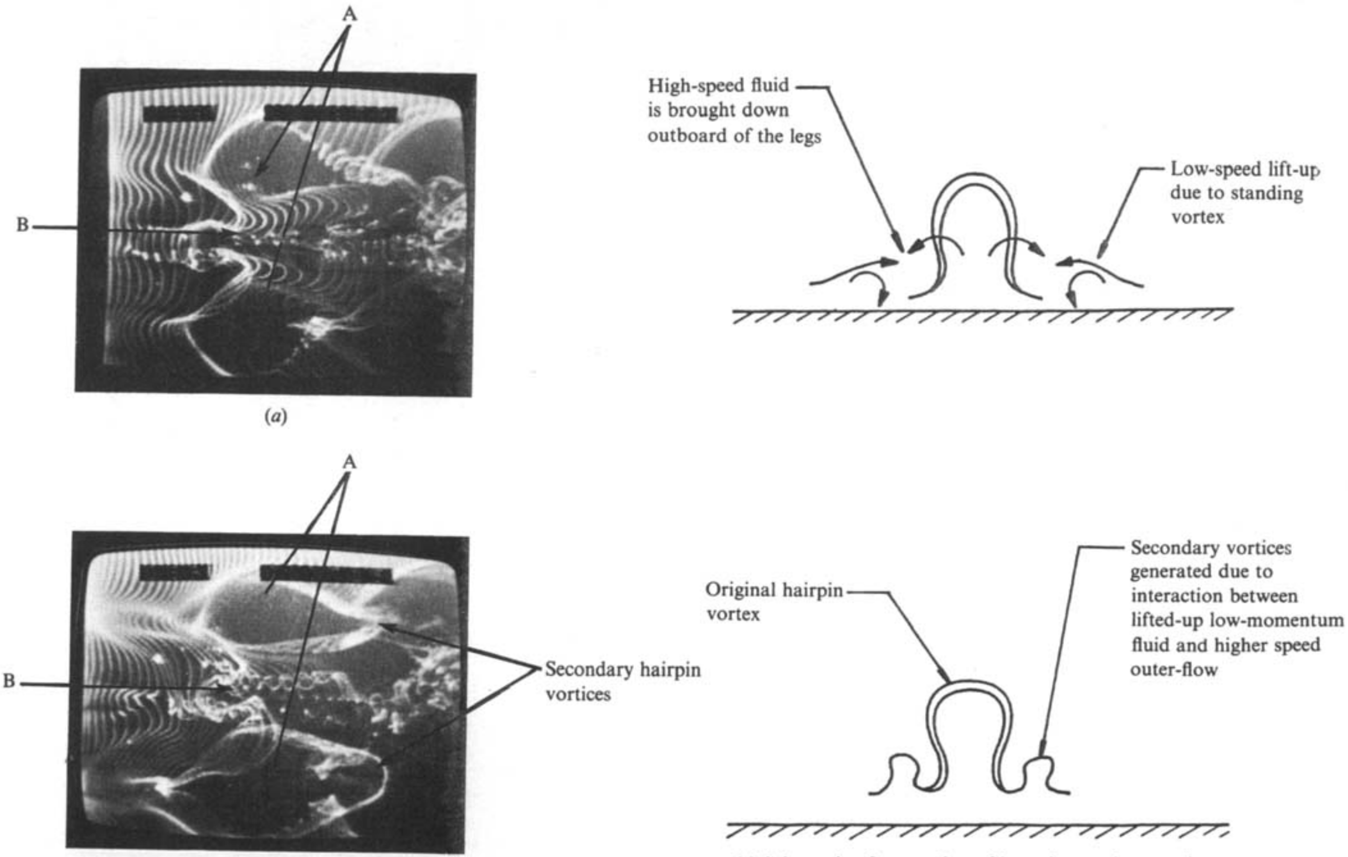

(*a*)

(*b*)

(*c*) Schematic of generation of lateral secondary vortices

FIGURE 17. Secondary flow patterns in the hemisphere wake. (*a*) Top view, $y/R = 0.638$, $x/R = 7.5$; (*b*) Top-view, $y/R = 0.465$, $x/R = 7.5$; (*c*) schematic of generation of lateral secondary vortices.

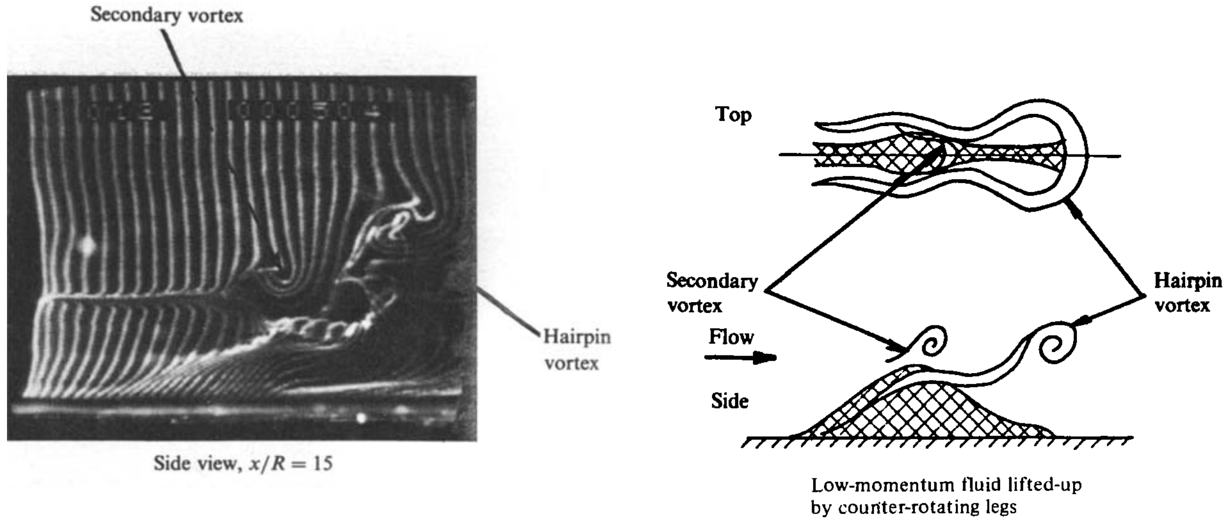

Side view, $x/R = 15$

FIGURE 18. Secondary vortex generated on the plane of symmetry due to shear-layer roll-up.

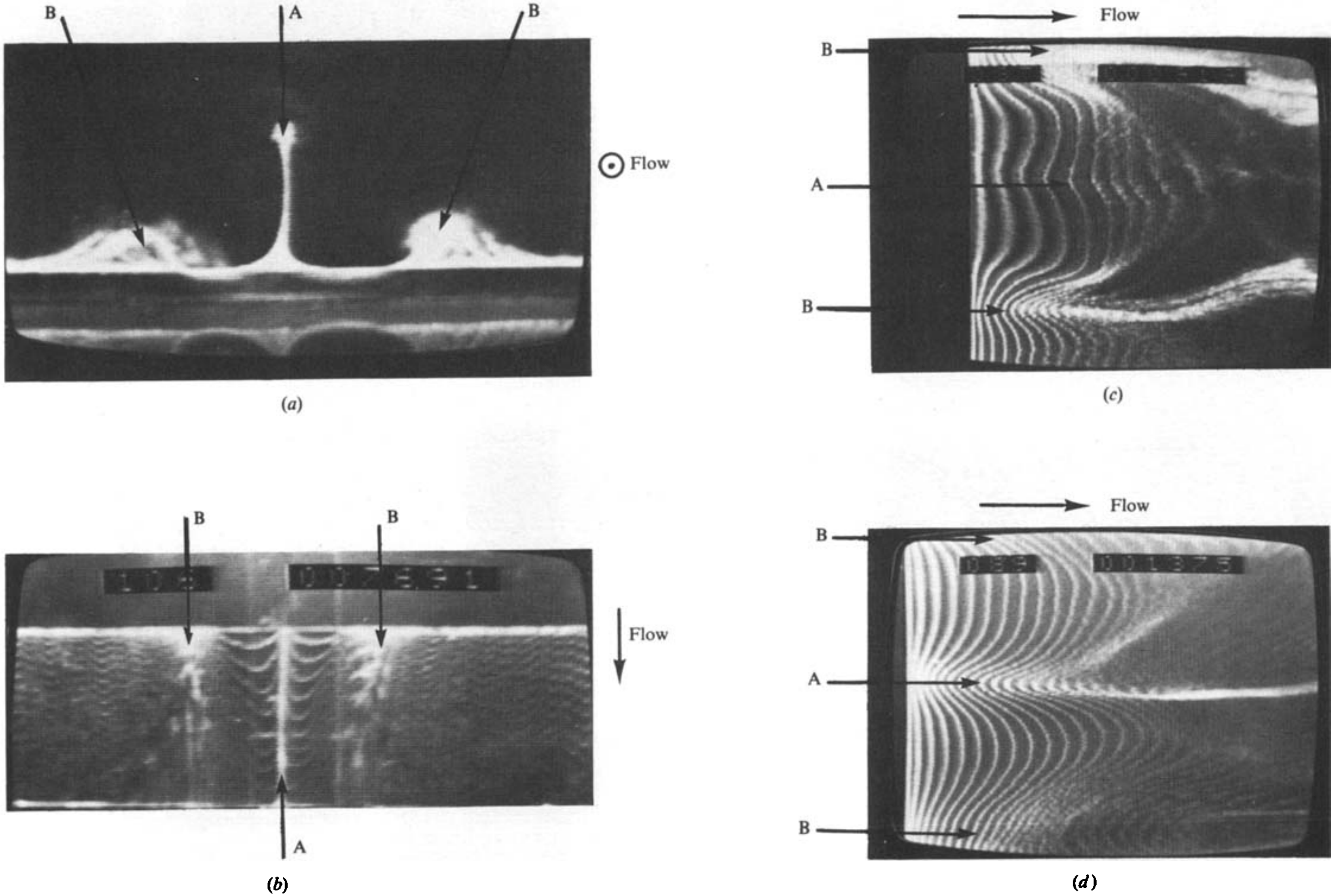

FIGURE 19. Far-wake bubble-line patterns. $Re_R = 900$. (*a*) End view of lifted-up low-momentum fluid between the counter-rotating streamwise legs: $x/R = 10$, $y/R = 0.1$. (*b*) Top view of (*a*): $y/R = 0.1$. (*c*) Top view: $x/R = 20$, $y/R = 0.25$. (*d*) Top view: $x/R = 45$, $y/R = 0.25$.

construed as turbulence. The effect of such an interaction on the velocity profile will be discussed in §7.

As shown in figure 13(*f*), the counter-rotating legs of the hairpin vortices generate narrow, low-speed concentrations by the lift-up and accumulation of low-momentum fluid between the legs. In order to examine the extent of these low-speed concentrations, a horizontal hydrogen-bubble wire was employed to visualize the flow characteristics close to the surface at a series of downstream locations. The visualization results are described below.

Figure 19(*a*) is an end-view visualization at a downstream location of $x/R = 10$ and bubble-wire height of $y/R = 0.1$. The hydrogen-bubble pattern clearly illustrates the lift-up of low-momentum fluid from the surface (labelled A) by the counter-rotating legs of the hairpin vortex. Flanking low-momentum regions (labelled B) also appear, created by a lift-up of wall-region fluid due to the standing vortex. Figure 19(*b*) is a corresponding top-view of the observed low-speed-fluid regions. The lifted, low speed fluid retards the bubble lines, forming bright kinks as observed in the top-view (note that the scales of figure 19(*a* and *b*) are different). Figure 19(*c, d*) are top views of the patterns observed near the wall at $x/R = 20$ and 45. It is clear that the low-speed regions maintain their integrity even at far-wake locations. It is worth noting that these low-speed patterns are very similar to the low-speed streak patterns commonly observed in the wall region of turbulent boundary layers. This point will be further examined in §9, where one-to-one comparisons between the patterns generated by hairpin vortices and the patterns observed in turbulent boundary layers are made.

## 7. Effect of hairpin vortices on velocity characteristics

Mean and fluctuating components of velocity in the streamwise direction were measured to determine the effect of the presence and evolution of hairpin vortices on the initially laminar boundary layer. The measurements were taken at a series of downstream locations using the hot-film anemometry and data acquisition system. Mean velocity profiles taken at several locations upstream of the hemisphere confirmed that the boundary layer was initially laminar (see Acarlar & Smith 1984).

In order to establish the effects of the developing hairpin vortices on the velocity field, dye was often used simultaneously as a visualization medium. The use of dye allowed specific velocity variations to be related to particular phases and portions of the developing hairpin vortices. Figure 20 illustrates the development of the mean and fluctuating components of the velocity profiles at four different downstream locations (4, 10, 40 and 80 *R*), on the plane of symmetry of the wake. The Reynolds number used based on the radius of the hemisphere is 750.

Examining figure 20(*a*), it is observed that a high-shear layer is reflected as a strong inflexion point in the mean velocity profile at a 4 *R* downstream location. This shear layer is generated due to the interaction between the low-momentum fluid lifted-up by the counter-rotating legs and the higher-speed flow of the boundary layer. The fluctuating component of the velocity demonstrates two distinct peaks: at $y/\delta = 0.27$ $(y/R = 0.5)$ and $y/\delta = 0.55$ $(y/R = 1)$. From the simultaneous dye and hot-film measurements these two peaks were determined to correspond to the locations where the probe intercepts (i) the transverse heads and (ii) the undulating, low-momentum fluid lifted-up by the counter-rotating streamwise legs. As the hot-film is moved downstream to $x/R = 10$ (figure 20*b*), the mean-velocity profile begins to flatten. At this downstream station the two peaks in the turbulence-

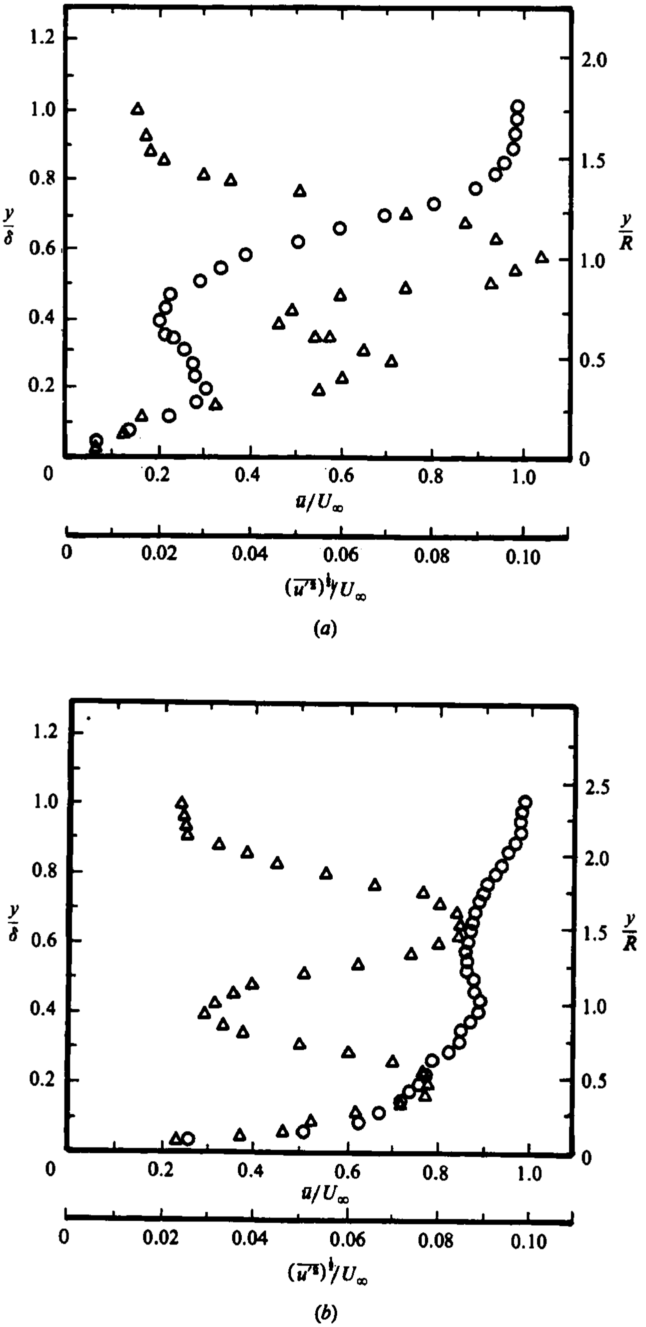

(a)

(b)

FIGURE 20 (a, b). For caption see facing page.

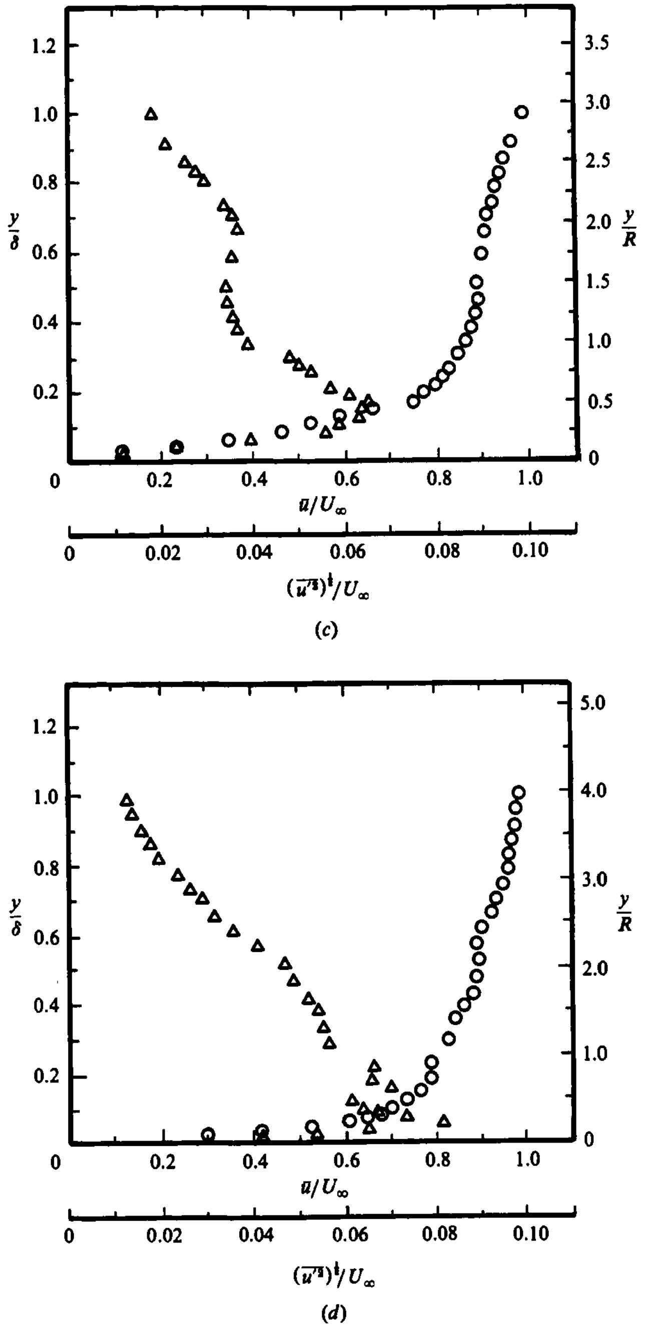

FIGURE 20. Velocity distribution in the wake of a hemisphere at the plane of symmetry. ○, $u/U_\infty$; △; $(\overline{u'^2})^{\frac{1}{2}}/U_\infty$; $Re_R = 750$; $R = 8.4$ mm ($u'$: fluctuating component of the streamwise velocity, $\bar{u}$: mean component of the streamwise velocity). (*a*) $x/R = 4$; (*b*) 10; (*c*) 40; (*d*) 80.

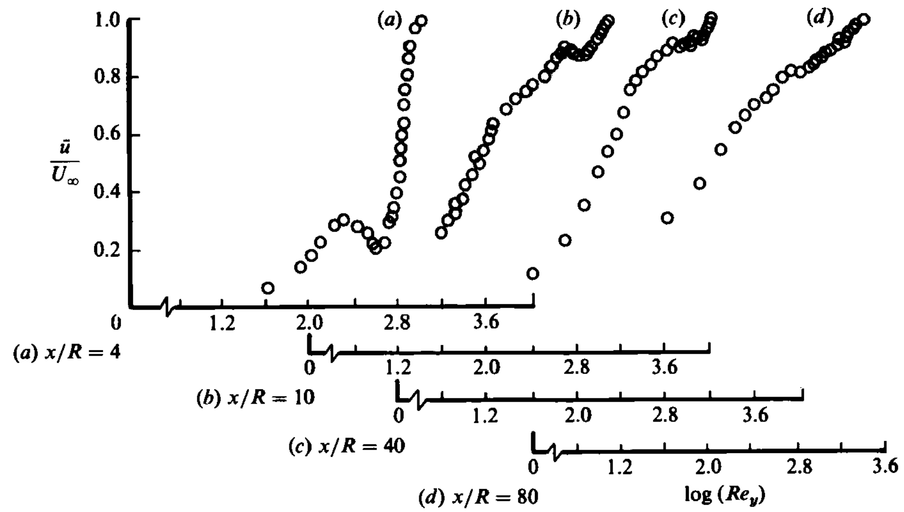

FIGURE 21. Law-of-the-wall Clauser cross-plot of mean-velocity data of figure 20, $Re_R = 750$.

intensity profile are still present, with the lower peak shifted slightly closer toward the surface and the upper peak shifted outward to $y/\delta = 0.65$ ($y/R = 1.5$), apparently owing to the head moving away from the surface as it convects downstream. At $x/R = 40$, figure 20(*c*), the kink in the mean-velocity profile has further flattened and the upper peak in turbulence intensity has rapidly diminished owing to diffusion of the head. Finally, by $x/R = 80$, figure 20(*d*), the mean-velocity profile displays only a slight residual kink; the upper peak in turbulence intensity has dissipated and the lower peak has migrated to very near to the wall.

Note that both profiles in figure 20(*d*) display a shape characteristic of a turbulent boundary layer. It has been shown (see Acarlar & Smith 1984) that increasing the free-stream velocity causes the velocity profiles to become fuller much earlier (i.e. closer to the hemisphere). Development of the turbulence-intensity profiles follows essentially the same trend as lower-velocity cases, with the peak value of turbulence intensity attaining a slightly higher maximum value.

The above mean-velocity data was also plotted on a Clauser-type cross-plot, as shown in figure 21, to determine if and when the velocity profiles display logarithmic behaviour characteristic of the law-of-the-wall equation:

$$\frac{u}{u_\tau} = 2.44 \ln y^+ + 4.9, \tag{1}$$

which characterizes wall-region turbulent velocity profiles. Substituting $u_\tau/u_\infty = (\frac{1}{2} cf)^{\frac{1}{2}}$ and rearranging (1) yields

$$\frac{u}{u_\infty} = C\left[5.618 \log\left(\frac{yu_\infty}{\nu} C\right) + 4.9\right], \tag{2}$$

where $C = (\frac{1}{2} cf)^{\frac{1}{2}}$. Equation (2) is in the form of

$$\frac{\bar{u}}{u_\infty} = A \log Re_y + B. \tag{3}$$

If the present data conforms to logarithmic behaviour, the data should yield a straight line on a semi-log graph. On examination of figure 21, the Clauser cross-plot of the hemisphere-wake data shown in figure 20, it is observed that at $x/R = 4$ the outer region of the mean-velocity profile yields a line almost parallel to the $\bar{u}/u_{\infty}$ axis. At progressively farther distances from the hemisphere, this somewhat straight portion of the velocity profile appears to rotate in a clockwise direction. By $x/R = 80$ the data appears to roughly conform to law-of-the-wall behaviour.

Visualization studies combined with the above hot-film results indicated that secondary instabilities and vortical structures (described in §6.4) occur owing to the breakdown of the hairpin vortices. The interaction between the secondary structures and the original hairpins appears to be the mechanism that creates the turbulent-type behaviour reflected in the measured velocity profiles. This point can be seen clearly from the evolution of the mean-velocity profiles of figure 21, which demonstrate the slow evolution of the velocity behaviour to a law-of-the-wall shape. Perry & Chong (1982) using theoretical arguments suggested that turbulent boundary layers consist of hierarchies of hairpins (older hairpins interacting with younger ones); they demonstrated that such a hairpin hierarchy can yield mean-velocity profiles that appear to fit the law-of-the-wall. This suggests that the hairpins generated by the hemisphere must develop secondary structures which interact with the original hairpins in order for the velocity profile to evolve into turbulent-type boundary-layer profile. The visualization data and hot-film measurements of figures 20 and 21 strongly support this view.

The visualization results described in §6 suggest that the three-dimensional coalescence of the legs of multiple hairpins results in a continued agglomeration of the streamwise vorticity from the legs of individual vortex loops into larger concentrations which appear to maintain their integrity and coherence in the presence of stretching and viscous dissipation. The extreme length of the low-speed streak-like concentrations near the surface also strongly supports this suggestion. Careful examination of figure 20 indicates that the lower $y/\delta$ turbulence-intensity peak never disappears and is present at every downstream location. The persistence of the high turbulence-intensity peak near the surface would seem to demonstrate that the counter-rotating legs continue their activity in spite of viscous dissipation. Note that the counter-rotating legs still appear to continue their activity at downstream locations where the transverse head appears to have essentially dissipated.

## 8. Geometric and rotational characteristics of hairpin vortices

Among the parameters that characterize the hairpin vortices are the core diameter $D_c$, circulation $\Gamma$, distance between the cores of the counter-rotating legs, and the geometric size and shape of the hairpin vortex at various downstream locations. There are a variety of experimental methods available to evaluate the above parameters for two-dimensional vortices and vortex rings, such as flow visualization, hot-film anemometry, and laser-Doppler velocimetry. However, owing to the variations of the characteristics of individual hairpins, the three-dimensionality of the flow, non-uniform stretching, and continuous evolution of the hairpin vortices, it is impractical, if not impossible, to determine circulation using LDV or hot-film-anemometry techniques. In the present study, dye and hydrogen-bubble visualization are used to determine the above parameters.

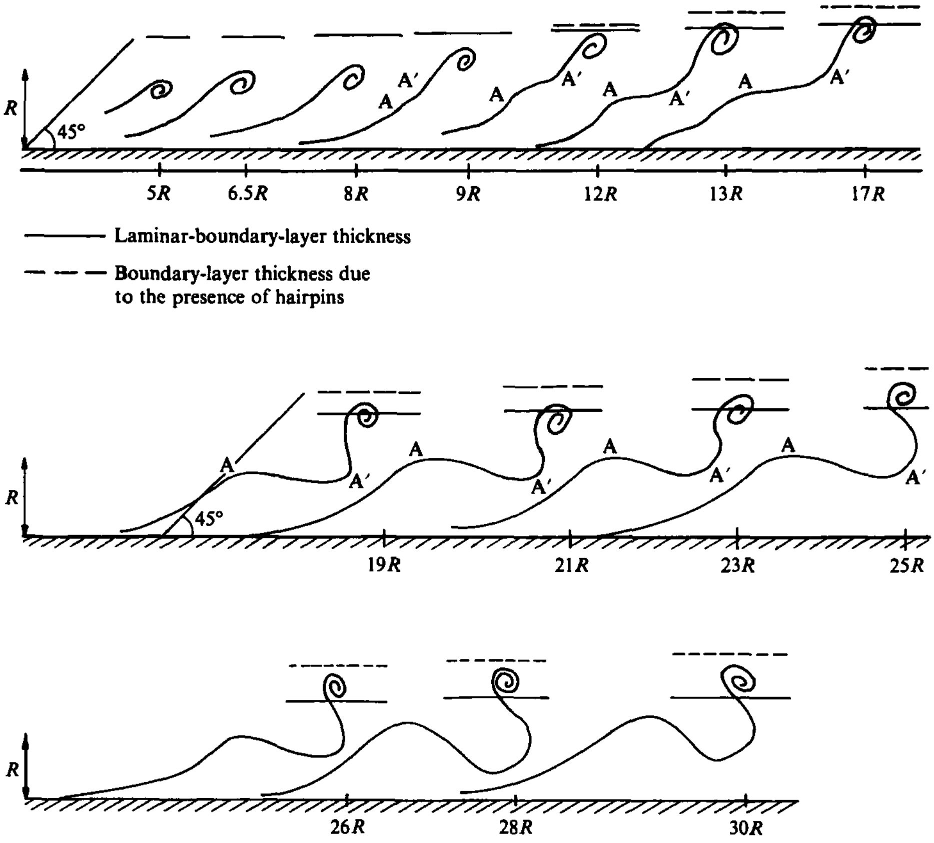

(a)

FIGURE 22(a). For caption see facing page.

### 8.1 *Geometrical evolution of hairpin vortices*

Once a hairpin vortex is generated, different portions of it stretch at different rates since mutual induction effects cause the various parts of the vortex to migrate through the surrounding boundary layer with its varying velocity gradient. Thus, a hairpin vortex will undergo a continuous evolution in shape and size. In the present study the geometric variations in the hairpin vortex at various downstream locations were determined using both hydrogen-bubble and dye visualization. The evolving hairpin shapes presented in figure 22(*a*) were obtained from a side-view dye-visualization sequence taken from a Lagrangian reference frame translating with the vortex (i.e. the dye patterns are for the *same* hairpin vortex obtained at a series of downstream locations). A traversing platform, which travels on two cylindrical steel rails mounted above and on either side of the channel support, was utilized for this purpose. The video cameras were mounted on this platform for viewing and recording of the visual data. The advantages of using a moving reference platform have been noted previously (Corino & Brodkey 1969; Smith 1978; Praturi & Brodkey 1978). Dye patterns were traced onto clear plastic sheets from a series of prints which were obtained using a video graphic printer (see Acarlar & Smith, 1984 for further details).

Figure 22(*a*) illustrates the evolution of the hairpin vortex as it progresses downstream. At the point of formation, the angle that the legs make with the wall is less than 10°. Mutual induction effects cause the forward portion of these legs and

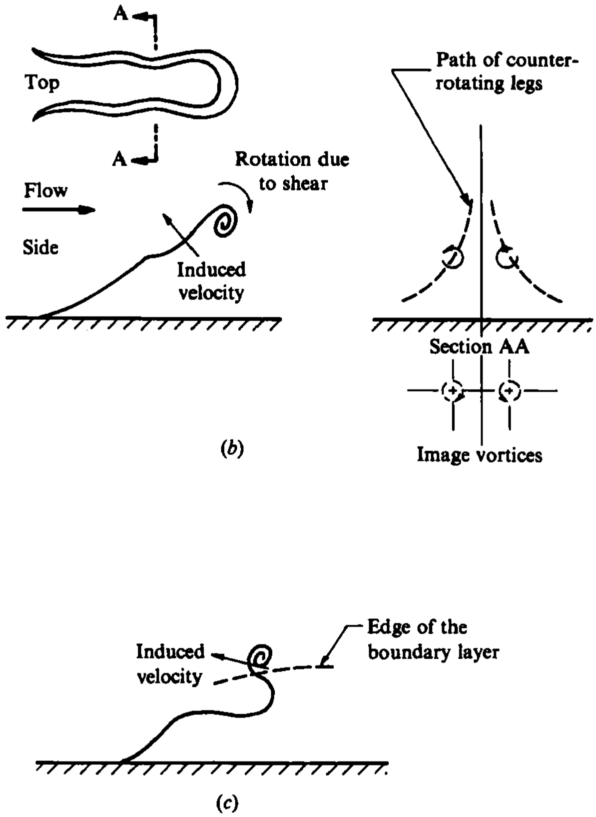

FIGURE 22. (*a*) Change of the size of a hairpin vortex at various downstream locations. $Re_R = 800$. (*b*) Schematic of the portion of the legs migrating together as they lift-up from the surface. (*c*) Curling back of the head when it is out of the boundary shear layer.

the head of the vortex to move away from the wall as shown in figure 22(*a*) (this begins between 5 and 8 *R* downstream from the hemisphere). Since the trailing portion of the legs must connect back to the lateral vorticity sheets (see figure 6), the trailing portions of the legs undergo extreme stretching by the local velocity gradient. This stretching further increases both the induced velocities and the concentration of vorticity in the core of the legs.

A portion of these legs, which move into outer regions because of mutual induction effects, migrate together owing to image-vortex effects as shown in figure 22(*b*). Since the legs are of opposite vorticity, as they approach each other they begin to interact through viscous effects such that mutual vorticity cancellation begins to take place (a process suggested by Head & Bandyopadhyay 1981).

Head & Bandyopadhyay (1981) suggest that a hairpin vortex in a shear layer will be under the influence of two opposing effects: a shear effect, which tends to rotate the hairpin back towards the wall, which is opposed by the induced velocity that each leg of the hairpin imposes upon the other. They suggest that the angle at which the hairpin reaches equilibrium will be the result of the interaction between these two opposing effects. It is believed that the reduction of the vorticity in the portions of the legs of the hairpin that closely approach each other will reduce the induced velocity of those parts of the legs, creating an imbalance towards the shear effect. A portion of the weakened legs will subsequently be pushed towards the wall by the shear flow, initiating a kinked region (labelled AA′) which is observed beginning at approximately 9 *R* in figure 22(*a*). As the mutual vorticity-cancellation effects proceed, the weakened portions of the legs (AA′) will rotate further towards the wall under the influence of the shear effect until they dissipate. This behaviour can also be observed in figure 12(*c–e*).

The growth of the head is also influenced by the rotation effect of the shear layer and an opposing induced velocity. The term 'growth' is used here to describe the combined visual effects of the movement of the head away from the surface due to (i) the mutual induction effects of the streamwise extentions of the head† and (ii) the increase in the size of the head due to diffusion of vorticity. The growth of the head does not continue beyond the edge of the boundary layer, but appears to continue only as long as the head remains in the shear layer. This observation is supportive of the previous suggestions of Head & Bandopadhyay (1981) regarding hairpin evolution. Once the head of the hairpin vortex is out of the boundary layer, it will only experience the effect of the induced velocity. This effect causes the tip to curl back upstream as illustrated in figure 22(*c*). Downstream of this point the head is affected only by viscous diffusion and advection by the free stream.

The portions of the legs that remain near the wall (between the wall and point A) maintain their integrity and develop strongly amplified vorticity concentrations as a result of the continuous stretching process. Head & Bandyopadhyay (1981) suggest that once a hairpin vortex has been rotated below an angle of 45°, the rate of stretching will decresae (45° is the direction of maximum strain for a shear flow). This decreased stretching will reduce induced flow effects, resulting in the hairpin being rotated toward the wall, under the influence of the shear effects, where it will dissipate. However, examination of figures 12 and 22(*a*) shows that this is not the case. Although the legs make angles smaller than 45° with the surface, they appear to maintain their integrity. It is believed that the persistence of the legs near the wall is a result of the three-dimensional coalescence of the legs of sequential hairpins. It is hypothesized that this coalescence of the legs results in a continued agglomeration of the streamwise vorticity from the legs of individual hairpins into larger concentrations which maintain their integrity and coherence in the presence of viscous dissipation.

### 8.2. *Core sizes*

The core sizes of the counter-rotating streamwise legs were established using end–top-view visualizations similar to those shown in §§6.1 and 6.3. The end view combined with the top view alleviated the problem encountered by Offen & Kline (1973) and Praturi & Brodkey (1978) of an inability to determine the sense of rotation of streamwise vortex structures when using a side- or top-view scheme alone. The core sizes of the standing vortex and the transverse tip were determined using a vertical hydrogen-bubble wire and side-view pictures. Hydrogen-bubble visualization is employed to determine the core sizes because of the drawbacks of the dye visualization. The major disadvantage of dye visualization for this application is that the entire region of developing vortical fluid is not shown by the dye in a vortex loop because the diffusion coefficient of dye is much smaller than the diffusion of the vorticity. The core diameters were measured both at the formation region of $x/R = 3$ and at a downstream location of $x/R = 5$. Measurements at further downstream locations were too uncertain owing to the continuous evolution and interaction of

---

† Note that the head of the hairpin (as defined in figure 3*b*) has streamwise components of vorticity.

hairpin vortices. A limited number of Reynolds-number cases were examined because of the difficulties with the visualization medium at higher velocities.

A typical end-view picture obtained using a horizontal hydrogen-bubble wire is shown in figure 9 at a downstream location of $x/R = 3$. It was determined that core diameters of the legs at this location are approximately 15 % of the diameter of the hemisphere at $Re_R = 800$. At $Re_R = 900$ the ratio was determined to be approximately 20 %. At a downstream location of $x/R = 5$ for $Re_R = 800$, the ratio was measured as 14 %. Figure 16, obtained at $x/R = 5$ and $Re_R = 800$, clearly demonstrates the size of the hairpin vortex and the distance between the counter-rotating legs, which was found to vary between $l/D = 0.5$ at $y/R = 0.54$ and $l/D = 0.2$ at $y/R = 0.13$.

A typical side-view picture used to determine the core sizes of the tip and the standing vortex is shown in figure 3(*a*). The ratio of the core diameter of the standing vortex to hemisphere diameter was determined to be 12 %. The ratio of core diameter of the tip of the hairpin vortex to hemisphere diameter was determined to be 18 %. Since the apparent (visible) diameter of the core (for the tip, legs and the standing vortex) continuously increases due to entrainment and diffusion, all the above measurements assume the minimum diameter marked by the bubble lines to be the 'actual' diameter.

### 8.3. *Vorticity and circulation of the hairpin vortices*

For selected cases, the vorticity of the tip ($\omega_z$), the streamwise legs ($\omega_x$), and of the standing vortex ($\omega_z$) were determined visually from the bubble-line patterns. It is assumed that various cross-sections of the hairpin and the standing vortex can be approximated as combined Rankine-type vortices. Outside the core, accurate determination of vorticity from the bubble-line patterns is not possible. Within the vortex core, it was assumed that $V_\theta = \Omega r$, where $\Omega$ represents the solid-body rotational speed. Vorticity $\omega$ was determined from bubble lines marking the core of the vortex by measuring the angle of rotation of a bubble line and the corresponding period over which that rotation takes place. The vorticity is non-dimensionalized on the velocity gradient at the wall:

$$\omega^+ = \left.\frac{2\Omega}{\partial u/\partial y}\right|_{\text{wall}} = \left.\frac{\omega}{\partial u/\partial y}\right|_{\text{wall}}. \tag{4}$$

Outside the core of a vortex, if the motion is asumed to be irrotational (as for a combined Rankine-type vortex), a line integral about the core will yield a value for circulation reflecting (essentially) the strength of the core alone.

Thus $$\Gamma \approx V_\theta \pi 2 r_c$$

and $$V_\theta = \Omega r_c, \tag{5}$$

where $r_c$ = radius at the point of measurement, and $\Omega$ = rotational velocity at $r_c$.

Thus $$\Gamma = \Omega 2\pi \rho_c^2 = \tfrac{1}{2}\pi_c^2 \Omega \tag{6}$$

with non-dimensional circulation given by

$$\Gamma^+ = \frac{\Gamma}{\nu}. \tag{7}$$

Using the above equations and procedure, the vorticity and circulation of the cores were determined for the head, counter-rotating legs, and the standing vortex at a $Re_R = 800$. All the magnitudes given below are mean values obtained from thirty measurements carried out for each case.

Figure 9(*c*) shows a bubble-line pattern illustrating the rotation of the vortex cores of the streamwise legs. For that sequence, an average value for the streamwise vorticity and circulation (from thirty measurements) were $\omega_x^+ = 0.88$ and $\Gamma_x^+ = 65$. For the sequence from which figure 3(*a*) is obtained, the vorticity of the standing vortex, $\omega_z^+$, is determined as $\omega_z^+ = 2.50$ and the circulation, $\Gamma_z^+ = 150$. $\omega_z^+$ and $\Gamma_z^+$ for the tip are obtained from the same sequence as $\omega_z^+ = 3.50$ and $\Gamma_z^+ = 430$. An uncertainty analysis for the above measurements showed that uncertainty of $\omega^+$ and $\Gamma^+$ are $\pm 14$ and $\pm 43\,\%$ respectively. From the above measurements, it is observed that the strength ($\Gamma^+$) of the counter-rotating legs is approximately one seventh of that of the tip. This is believed to be due to the mutual vorticity-cancellation effects that the counter-rotating legs impose on each other through viscous interaction. This effect tends to reduce the vorticity concentrated in the core of the legs. Note that for the transverse head there is no similar mechanism by which the transverse vorticity in the hairpin tip can be reduced (it will diffuse, but cannot undergo a cancellation).

The above results also show that the circulation of the standing vortex (measured upstream of the hemisphere) is one-third that of the head. This difference is believed to be due to the existence of the inflexion point (i.e. maximum vorticity) at the point of formation of the head. The inflexion point is observed to occur at a height of $y/R = 1$ (also the formation region of the transverse head) as shown in mean velocity profile of figure 19(*a*). Since the transverse head is formed from the concentration of vortex lines, which represent the region of maximum vorticity (point of inflexion), it is expected that the vorticity (i.e. the vorticity concentration at a height of $y/R = 1$) and circulation of the head will be larger than the standing vortex, which has its origin in a region where velocity gradients are weaker.

Because of the difficulties associated with the data measurements (due to the continuous stretching and evolution of hairpin vortices), and the variation in the data, it was not considered practical to determine circulation using the hydrogen-bubble method for a large Reynolds-number range. Additionally, there are at least three sources of error in the bubble-method calculation besides the normal measurement error. The first possible source is that the bubble velocity may not be the same as that of the fluid. Although this error is not evaluated, Schraub *et al.* (1965) showed that it should be negligible after the bubble line is reasonably removed from the generating wire. A second source of error is the presence of vorticity outside the vortex core. The third source is the difficulty in determining the exact centre and diameter of the core.

It appears that, owing to the transient three-dimensionality of the hairpin vortex, no experimental technique at present is sufficient for the accurate measurement of the vorticity.

## 9. Comparison of hemisphere wake patterns with turbulent-boundary-layer patterns

To further emphasize the similarity between the bubble-line patterns generated by hairpin vortices and those observed in the near-wall region of turbulent boundary layers, figures 23, 24 and 25 are shown. Figure 23(*a*) is a side-view picture of a hairpin-vortex pattern obtained with a vertical bubble wire located 20 radii downstream from the generating hemisphere. Figure 23(*b*) is a dual side-view picture of a turbulent boundary layer with a wider view of the general boundary-layer behaviour superposed above a second, more magnified view of the near-wall region

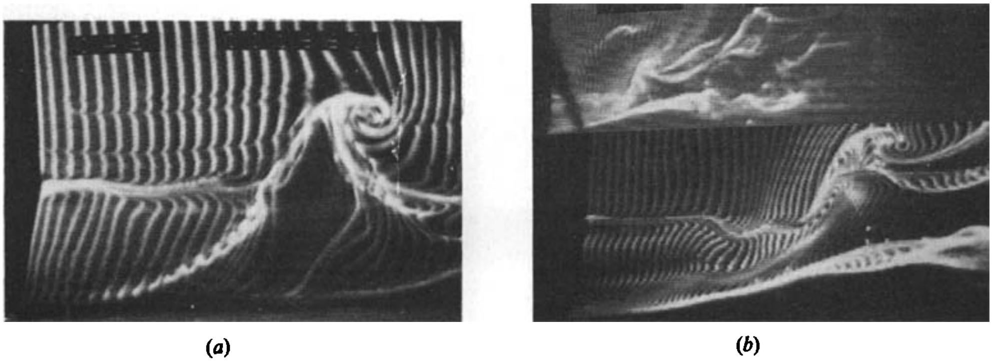

FIGURE 23. Side-view comparison between hairpin vortex and turbulent-boundary-layer patterns. (a) Hairpin vortex, $x/R = 20$; (b) Turbulent boundary layer, $Re_\theta = 2200$.

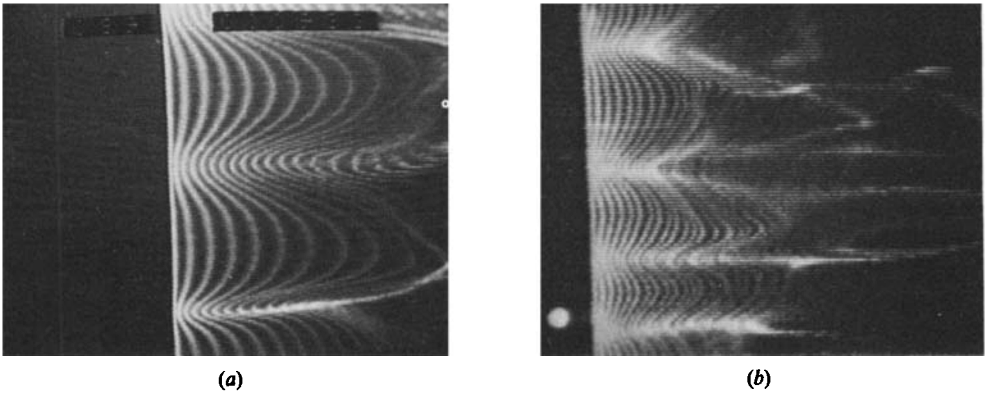

FIGURE 24. Top-view comparison between hairpin vortex and turbulent-boundary-layer pattern. (a) Hairpin vortex, $x/R = 20$, $y_{\mathrm{wire}}/R = 0.08$; (b) Turbulent boundary layer, $Re_\theta = 2200$, $y^+_{\mathrm{wire}} = 5$.

exclusively. Comparison of the vortical pattern of figure 23(*a*) with the very similar pattern shown in the near-wall region (bottom-view) of figure 23(*b*) appears to leave little question that the bubble-line patterns are created by essentially the same type of flow structure.

Figure 24(*a*) is a top-view bubble-line pattern created by a hairpin vortex passing over a horizontal bubble-wire again 20 radii downstream of the hemisphere. The bright bubble concentrations are regions of low-momentum fluid lifted away from the surface by the counter-rotating legs of a hairpin vortex (the middle concentration) and streamwise extensions of the standing vortex (the two lateral concentrations). A detailed description of the formation kinematics with the supporting end-view was presented earlier in figure 19(*a*). Figure 24(*b*) is a hydrogen-bubble-line visualization of the low-speed streak pattern characteristic of the near-wall region of a turbulent boundary layer. The striking similarity between the two pictures strongly supports the suggestion that low-speed streaks of turbulent boundary layers are generated by low-momentum fluid lifted up between the counter-rotating legs of hairpin-type vortices.

Figure 25(*a*) is obtained with bubble wire at the same downstream location as figure

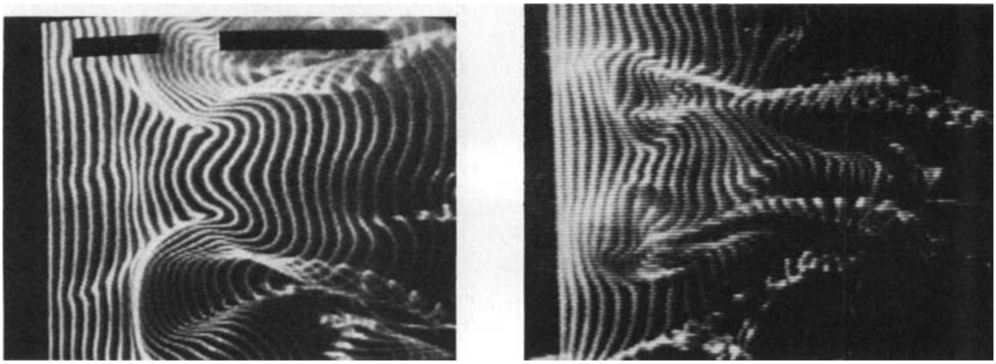

FIGURE 25. Top-view comparison between hairpin vortex and turbulent boundary layer pattern with bubble wire at same downstream location as figure 24 but further from the surface. (*a*) Hairpin vortex, $x/R = 20$, $y_{\mathrm{wire}}/R = 0.25$; (*b*) Turbulent boundary layer, $Re_\theta = 2200$, $y^+_{\mathrm{wire}} = 30$.

24(*a*), but farther from the surface. This figure reveals two pocket-like patterns connected to streamwise vortical structures which mark the location where the counter-rotating legs cross the bubble-line-generation plane. Figure 25(*b*) is a bubble-line pattern obtained in a turbulent boundary layer at a bubble-wire height of $y^+ = 30$. Again the similarities between the two pictures (although the scales are different) are quite obvious.

## 10. Summary and discussion

The hot-film-anemometry studies have shown that the vortex shedding from a hemisphere within a laminar boundary layer displays a periodic behaviour in the Reynolds-number range of $120 < Re_R < 3400$.

Near-wake visualization studies revealed that two kinds of vortices are formed owing to the interaction of an initially laminar boundary layer with a hemisphere protuberance. The first is a standing vortex, which is generated at the upstream stagnation point of the hemisphere. This is a stable vortex pattern which follows the contours of the hemisphere. The second vortex structure is a hairpin-type vortex which periodically sheds into the wake of the hemisphere. The generation of these two kinds of vortices is explained and described in terms of vorticity concentrations. Dual-view visualization studies further aided in understanding and explaining the details of the formation of these vortices.

From the results presented in the present study, it is clear that the flow patterns observed in the hemisphre wake display a wide variation in appearance depending on the type and method of introduction of visualization medium. The types of patterns were classified and the actual portions of the flow structures that cause the formation of the visualized patterns were deduced from slow-motion review of recorded video sequences. A summary of the evolution process of a hairpin vortex is given below.

Once a hairpin vortex is formed, its transverse tip, head and counter-rotating legs begin to move away from the wall owing to mutual induction effects, as shown schematically in figure 22(*b*). The hairpin vortex aligns itself at 45° to the wall during this stage (as shown in figure 12*a*). As the hairpin rises, the upper portions of the legs migrate across the boundary-layer velocity gradient which results in a stretching of the legs. This stretching process increases the concentration of vorticity in the core of the legs, which causes the legs to move rapidly together due to image-vortex effects. The portions of the legs that merge together begin to interact via viscous effects reesulting in a mutual vorticity cancellation, which is reflected as a weakening of the vorticity in those portions of the legs in closest proximity to each other. The result is the development of a kink in the vortex legs, shown schematically in figure 22(*b*). A hairpin vortex in a bounded shear layer is under the influence of both (i) the shear flow, which tries to rotate the hairpin towards the wall; and (ii) mutually induced velocities, which try to lift the hairpin away from the wall. Reduction of the vorticity in the merged region of the legs results in a decrease in the induced velocities of these portions. Once the balance is destroyed, the kink further develops and is gradually rotated towards the wall under the influence of the shear, as shown in figures 22(*c*) and 12(*c*) (labelled as AA′). As the mutual vorticity-cancellation effects proceed, the weakened portions of the legs rotate further towards the wall until they dissipate.

The growth of the hairpin head appears to continue as long as the head is in the boundary layer. Once the head passes out of the boundary layer, it will only be under the influence of its own induced velocity and free-stream advection. The induced-velocity effect causes the tip of the head to curl back as shown in figure 21(*c*) (also figure 12*c*–*e*). The trailing portions of the legs, which connect back to transverse vortex lines flanking the near-wall region, continue to be stretched by the velocity gradient, thus maintaining their integrity and coherence.

The legs and heads of multiple hairpins appear to coalesce in a three-dimensional fashion during the early stages of the evolution process (between 3 and 8 $R$ downstream of the hemisphere for $Re_R = 810$, as shown in figure 12*a*). This apparent coalescence of the legs and the heads of consecutive vortices appears to increase the coherence and vorticity concentration of the heads of individual vortices, precipitating a sudden movement of the head upward and downstream owing to vortex-induction effects (similar to the 'leap-frogging' behaviour observed to occur between two axially aligned vortex rings in close proximity).

The local viscous flow behaviour induced by the presence of the hairpin vortices is responsible for the development of two important flow structures. The first of these is the low-speed streak-type structure which appears near the wall (as shown in figures 19 and 24*a*). It was observed that the low-speed regions can be created by either (i) a low-momentum fluid concentration which is lifted-up by the counter-rotating legs of the hairpin vortices, or (ii) low-speed concentrations flanking the hairpin vortex generated by low-momentum fluid which is lifted-up by the streamwise extensions of the standing vortex (as shown in figures 8 and 9*c*). The second type of flow structures that appear to be associated with the development of hairpins are secondary vortices. These structures appear to be generated by the roll-up of strong shear layers which develop between the low-speed lifts-ups and the higher-speed, outer boundary-layer flow (see figures 17 and 18). Hot-film-velocity measurements combined with dye-visualization techniques show that the presence of the hairpin vortices and secondary vortices give rise to mean-velocity profiles which appear to evolve toward turbulent profiles.

From the results of this study a much broader and more detailed understanding of the complex behaviour of hairpin vortices has been gained. It has been demonstrated that a wide variety of visual patterns can be created by a simple hairpin vortex, depending upon the degree to which the hairpin has evolved and the location of the bubble wire. By use of this 'catalogue' of patterns, it appears possible to detect and track the presence of such hairpin-vortex structures in fully developed turbulent-boundary-layer flows. The striking comparison between the flow patterns generated by the presence of discrete hairpin vortices and the patterns observed in the near-wall region of turbulent boundary layers strongly suggests that hairpin vortices are a basic flow structure of turbulent boundary layers; however, the origin of hairpin vortices within turbulent boundary layers is unclear. Previous studies of turbulent boundary layers (e.g. Kline *et al.* 1967; Smith 1984) have suggested that the breakdown of low-speed streaks in the near-wall causes the generation of the hairpins in turbulent boundary layers. To investigate this suggestion for the origin of the hairpin vortices in turbulent boundary layers and their role in turbulence processes, a study has been done which examines the breakdown of a synthetic low-speed streak generated by continuous injection of fluid through a streamwise slot. It is determined that the breakdown of the synthetic streak yields a periodic train of hairpin vortices over a wide range of flow conditions (Acarlar & Smith 1984). The details of this study are published in a companion paper (Acarlar & Smith 1987).

The authors wish to thank Dr J. David A. Walker and Mr A. Haji-Haidari for their advice and assistance. We also wish to thank the Air Force Office of Scientific Research for its support of this research. The continuing support of the AFOSR is gratefully acknowledged.

## REFERENCES

ACARLAR, M. S. & SMITH, C. R. 1984 An experimental study of hairpin-type vortices as a potential flow structure of turbulent boundary layers. *AFOSR Rep.* FM-5, Dept. of Mech. Engrg. and Mech., Lehigh University, Bethlehem, PA.

ACARLAR, M. S. & SMITH, C. R. 1987 A study of hairpin vortices in a laminar boundary layer. Part 2. Hairpin vortices generated by fluid injection. *J. Fluid Mech.* **175**, 43–83.

ACHENBACH, E. 1974 Vortex shedding from spheres. *J. Fluid Mech.* **62**, 209–221.

BOGARD, D. G. 1982 Investigation of burst structures in turbulent channel flows through simultaneous flow visualization and velocity measurements. Ph.D. dissertation, Dept. of Mechanical Engineering, Purdue University.

CORINO, E. R. & BRODKEY, R. S. 1969 A visual investigation of the wall region in turbulent flow. *J. Fluid Mech.* **37**, 1–30.

DRYDEN, H. L. 1953 Review of the published data on the effects of roughness on transition from laminar to turbulent flow. *J. Aero. Sci.* **20**, 477–82.

FALCO, R. E. 1981 Structural aspects of turbulence in boundary layer flows. *Proc. 6th Biennial Symp. on Turbulence* (ed. G. K. Patterson & J. L. Zakin). Dept. of Chem. Engng, University of Missouri, Rolla.

HALL, G. R. 1967 Interaction of the wake from bluff bodies with an initially laminar boundary layer. *AIAA J.* **5**, 1386–92.

HEAD, M. R. & BANDYOPADYAY, P. 1981 New aspect of turbulent boundary-layer structure. *J. Fluid Mech.* **107**, 297–337.

KLEBANOFF, P. S. 1955 Measurements of the effect of two-dimensional roughness elements on boundary layer transition, *J. Aeron. Sci.*, November, pp. 803–804.

KLEBANOFF, P. S., TIDSTROM, K. D. & SARGENT, L. M. 1962 The three-dimensional nature of boundary-layer stability. *J. Fluid Mech.* **12**, 1–34.

KLINE, S. J., REYNOLDS, W. C., SCHROUB, F. A. & RUNSTADLER, P. W. 1967 The structure of turbulent boundary layers. *J. Fluid Mech.* **30**, 741.

MAXWORTHY, T. 1972 The structure and stability of vortex rings. *J. Fluid Mech.* **51**, 15–32.

METZLER, S. P. 1982 Processes in the wall region of a turbulent boundary layer. M.S. thesis, Dept. of Mech. Engng. and Mech., Lehigh University.

Mochizuki, M. 1961*a* Smoke observation on boundary layer transition caused by a spherical roughness element. *J. Phys. Soc. Japan.* **16**, 995–1008.

Mochizuki, M. 1961*b* Hot-wire investigations of smoke patterns caused by a spherical roughness element. *Nat. Sci. Rep., Ochanomizu University*, vol. 12, no. 2, pp. 87–101.

Möller, W. 1938 Experimentelle Untersunchung zur Hydromechanik der Kugel. *Z. Phys.* **39**, 57–80.

Mujumbar, A. S. & Douglas, W. J. M. 1970 Eddy shedding from a sphere in turbulent free streams. *Intl J. Heat Mass Transfer* **13**, 1627–1629.

Offen, G. R. & Kline, S. J. 1973 Experiments on the velocity characteristics of 'bursts' and in the interactions between the inner and outer regions of a turbulent boundary layer. *Rep.* MD-31, Stanford University.

Perry, A. E. & Chong, M. S. 1982 On the mechanisms of wall turbulence. *J. Fluid Mech.* **119**, 173–217.

Perry, A. E., Lim, T. T. & Teh, E. W. 1981 A visual study of turbulent spots. *J. Fluid Mech.* **104**, 387–405.

Praturi, A. K. & Brodkey, R. S. 1978 A stereoscopic visual study of coherent structures in turbulent shear flow. *J. Fluid Mech.* **89**, 251–72.

Schraub, F. A., Kline, S. J., Henry, J., Runstadler, P. W. & Littel, A. 1965 Use of hydrogen bubbles for qualitative determination of time dependent velocity fields in low-speed water flows. *Trans. ASME* D: *J. Basic Engng.* **87**, 429–444.

Smith, C. R. 1978 Visualization of turbulent boundary layer structure using a moving hydrogen bubble wire probe. *Lehigh Workshop on coherent Structure in Turbulent Boundary Layers* (ed. C. R. Smith & D. E. Abbott, pp. 48–97.

Smith, C. R. 1984 A synthesized model of the near-wall behaviour in turbulent boundary layers. *Proc. 8th Symp. on Turbulence.* (ed. G. K. Patterson & J. L. Zakin). Dept of Chem. Engrg., University of Missouri, Rolla.

Taneda, S. 1956 Experimental investigation of the wake behind a sphere at low reynolds numbers. *J. Phys. Soc. Japan.* **11**, 1104–1108.

Tani, I. 1961 Effect of two-dimensional and isolated roughness on laminar flow. In *Boundary Layer and Flow Control*, vol. 2, pp. 637–656. Pergamon.

Tani, I. 1981 Three-dimensional aspects of boundary-layer transition, *Proc. Indian Acad. Sci.* **4**, 219–238.

Torobin, L. B. & Gauvin, W. H. 1959 Fundamental aspects of solids-gas flow. Part II. The sphere wake in steady laminar fluids. *Can. J. Chem. Engng* **37**, 167–176.

Utami, T. & Ueno, T. 1979 Lagrangian and Eularian measurement of large scale turbulence by flow visualizing techniques. In *Flow Visualization.* (ed. T. Asanunra), p. 221. Hemisphere.

Wille, R. 1972 Generation of oscillatory flows. In *Flow Induced Structural Vibrations* (ed. E. Naudascher), pp. 1–16. Springer.